
Interface characterisation in SiGe/Si/SiGe multilayers using atom probe tomography

EXTERNAL INTERNSHIP REPORT

Author:

Y. Baron
0936539

External supervisors¹:

Dr. J. E. Scheerder
Prof. Dr. C. Fleischmann

TU/e supervisor²:

Prof. Dr. P.M. Koenraad

¹imec: Materials and Component Analysis, Kapeldreef 75, 3001 Leuven, Belgium

²Department of Applied Physics: Photonics and Semiconductor Nanophysics



August 1, 2022

15 EC External internship as part of a double program Applied Physics (Bio/Nanoscience and Technology track) and Electrical Engineering (Photonic Integration group)

This thesis is public and Open Access.

Abstract

The quantum computer has the potential to outperform the classical computers in a variety of areas, stimulating the continues work on its development. One of the key components to be developed is the qubit. Similar to the transistor in the classical computer, this component will form the basic building block for the quantum computer. Silicon based platforms have emerged for the creation of the qubit due to the long spin coherence lifetime and the well-established silicon based fabrication processes. The performance of these components crucially depends on the Si/SiGe interfaces used to confine the electron. Therefore, a measurement technique to characterize these buried interfaces is required, for which atom probe tomography is a possible candidate. Atom probe tomography has the ability to provide three-dimensional information about buried interfaces, although it relies on a non-trivial tomographic reconstruction protocol which may induce artifacts and errors in the characterisation. Additionally, this protocol is reliant on various reconstruction parameters to be provided by the user that can often not be unequivocally defined. In this work, the influence of inaccuracies in the reconstruction on the interface characterisation are examined. Parameters which are examined are the chemical interface roughness and the transition width of the Si/SiGe interfaces. In an attempt to increase the confidence in choosing the values of the reconstruction parameters, the applicability of a method to calibrate these parameters based on the crystallographic information present in the APT data is investigated. Although the applied filtering method unveiled a novel pattern in the detector event histogram of a Si sample, it has been found that the crystallography could not directly be used during the calibration of the SiGe/Si/SiGe reconstruction. Hereafter, the reconstructed volume is checked and corrected for the presence of the well-known density artifacts by comparing a top-down and backside measurement. The density artifacts are shown to have a substantial impact on the interface characterisation, which is reduced after a density correction has been applied. The influence of a different choice of one of the construction parameters (i.e. the image compression factor) on the interface characterisation is provided, showing that the interface characterisation strongly depends on the reconstruction parameters. With the insights provided in this report, some of the potential pitfalls during the reconstruction and interpretation of the data for the characterisation of buried interfaces may be avoided.

Contents

1	Introduction	1
2	Atom probe tomography: the fundamentals	3
2.1	The theory of field evaporation	3
2.2	Atom probe setup	5
2.3	Samples and sample preparation	6
2.4	APT data and reconstruction	7
2.5	Artefacts and corrections	9
3	Data analysis	10
3.1	Application of the reconstruction protocol	10
3.2	Interface characterisation	11
4	Crystallography for reconstruction calibration	13
4.1	Crystallography in APT data	13
4.2	Retrieving crystallographic information	15
5	Influence of density artifacts on interface characterisation	21
6	Deviations due to varying the reconstruction parameters	26
7	Discussion and conclusion	29
8	Bibliography	31

1 | Introduction

The quantum computer can potentially provide great benefits over classical computers in a variety of areas. These foreseen benefits stimulate the ongoing work on its development. One of the key components to be developed is the qubit, which forms the basic building block of the quantum computer. This component shares many similarities to the transistor, but it operates in the single electron regime [1, 2]. The advancements in classical microelectronics of the last decades have predominantly been based on silicon technologies, which has led to the establishment of well-defined silicon based production methods and extensive research into the various properties of silicon. Now, next to its benefits to microelectronics, silicon is identified as a promising platform for spin-based quantum-information processing, because of the existence of isotopes with zero nuclear spin [3]. This is a desirable characteristic as it leads to long spin coherence times [4], which is an important property for many quantum applications [5]. However, bulk silicon has a six fold degenerate conduction band minimum, leading to an uncontrolled degree of freedom [3]. In one of the main platforms that have emerged, electrons are confined in a Si quantum well by SiGe barriers [2]. The in-plane strain induced by the SiGe layers reduces the conduction band minimum to a two-fold degeneracy [3]. By the confinement of the electron in the well and the applied electric fields, the remaining degeneracy is lifted. The breaking of this two-fold degeneracy is strongly influenced by the atomic-scale structure of the Si/SiGe interfaces, while a large splitting of the degenerate conduction band minimum is desired. A careful control over the interfaces during fabrication is thus crucial to the performance of the qubit.

With the use of atom probe tomography (APT), these buried interfaces can be revealed and, therefore, the influence of various fabrication conditions can potentially be mapped and linked to the final qubit performance. APT is a measuring technique that can visualize needle-shaped specimens in all three spatial dimensions [6]. Using a voltage or laser pulse superimposed on a constant electric field, the atoms at the surface of the specimen can be ionized and accelerated towards a position-sensitive detector. By using a time-of-flight (TOF) measurement, the chemical nature of each atom can be determined. Even though APT is capable of detecting the various constituents of the sample, a tomographic reconstruction protocol is required to convert the two-dimensional detector hit coordinates and the evaporation sequence to a three-dimensional image of the specimen [7]. An example of a reconstructed specimen can be seen in Figure 1.1, where the points represent the reconstructed positions of Si and Ge ions. Defining a reconstruction protocol is not trivial and the assumptions made during the reconstructions may influence the resulting parameters used to characterize the interfaces. For example, a well-known artifact is the density fluctuations observed near interfaces between different materials [8–10]. This artifact may be corrected for by using a density correction [8]. Additionally, the accuracy of the reconstruction depends on a number of reconstruction parameters, which are defined by the user. Due to the lack of a standardized protocol to chose these parameters, there

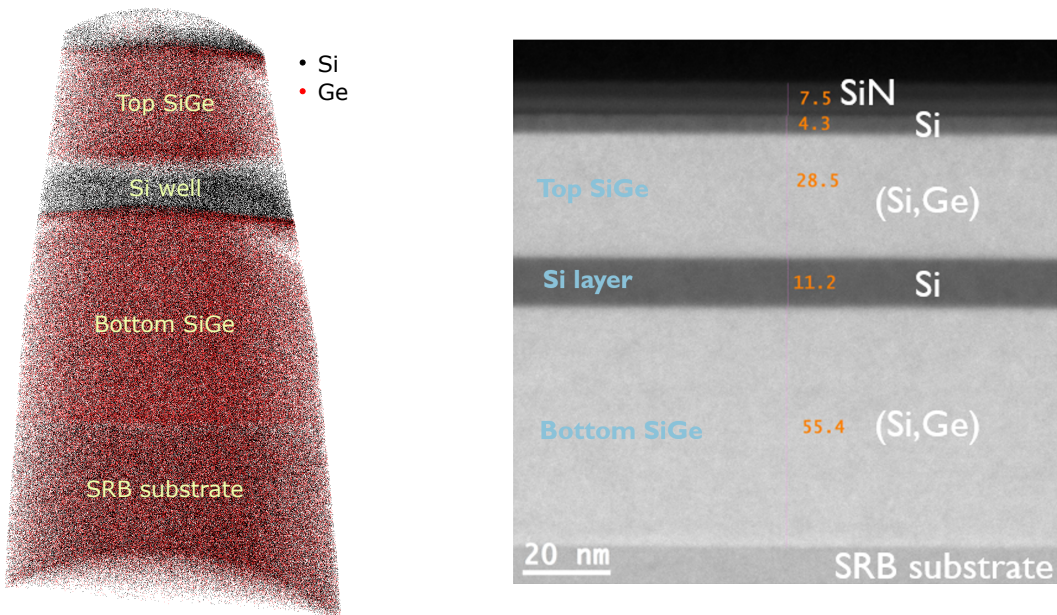


Figure 1.1: In the left image, the 3D point cloud can be seen as created by reconstructing the needle-shaped specimen from the APT data. Only 4% of the detected Si atoms and 8% of the detected Ge atoms are presented in this image to enhance the visibility. Other measured chemical entities are not shown. A TEM image of the used multilayer is shown on the right. The layers are labeled and the layer thickness is given in nm.

may be observable differences between reconstructions done by different users.

APT has previously been used to characterize SiGe/Si/SiGe multilayers [11–13]. This work aims to examine the reliability of APT to characterize the buried interfaces in these multilayers. The root mean square (rms) roughness, mean roughness and the transition width between the SiGe/Si interfaces are considered. The ultimate goal is to determine the differences of these interfaces between samples prepared under various processing conditions (e.g. the post annealing) and to link the found parameters to the qubit performance. A transmission electron microscopy (TEM) image of the SiGe/Si/SiGe multilayer used during this work can be seen in Figure 1.1. No further annealing steps have been applied to this sample. At first, it is evaluated whether the crystallographic information present in the APT data can be utilized to calibrate the input parameters for an optimal reconstruction. In this way, a better founded choice could potentially be made for the reconstruction parameters, reducing the variability of the reconstruction between users. Hereafter, the effect of the density artifact on the characterisation of the interfaces is quantified and the impact of the density correction is tested. As a final step towards the mentioned goal, the influence of a slight change in one of the reconstruction parameters on the interface characterisation is provided.

This report is build up as follows: In the Chapter 2 of this report, the fundamentals of atom probe tomography will be discussed. Hereafter, in Chapter 3, the steps taken to obtain the interface parameters (i.e. the transition width and chemical interface roughness) are described. The assessment of the usability of the crystallographic structure is provided in Chapter 4, which is followed by the quantification of the impact of the artifacts and the density correction in Chapter 5. As a final result, the influence of one of the input parameters of the reconstruction, the so-called ICF, is given in Chapter 6. A discussion and conclusion of the findings presented in this report is given in Chapter 7. An outlook is also provided.

2 | Atom probe tomography: the fundamentals

Atom probe tomography (APT) is a materials characterization technique capable of obtaining three-dimensional information of atomic positions and their elemental origins. During an atom probe measurement, atoms are field evaporated in a controlled manner from the surface of a needle-shaped sample. This chapter starts by describing the theory of field evaporation, after which a brief overview is provided of the various components of the APT setup and the basic considerations made during a measurement. A description of the used samples and the sample preparation is provided in Section 2.3. In order to convert the 2D spatial information acquired after an APT measurement to a 3D image of the sample, a reconstruction protocol needs to be applied. This 3D image comes in the form of a point cloud, where the points represent the ion locations. In Section 2.4 such a protocol is described. In the final section of this chapter, the possible problems associated with an inexact reconstruction are briefly introduced. Some methods will be provided to decrease the known artifacts.

2.1 The theory of field evaporation

Atom probe tomography relies on the controlled field evaporation of atoms from the sample surface. This entails the ionisation of an atom subjected to a high electric field, followed by the desorption of the created ion. While the electron propagates into the surface, the ion is accelerated by the electric field away from the surface towards a detector [7]. Although an exact quantum mechanical description has yet to be developed, several models have been proposed of field evaporation [14, 15]. The most comprehensible description of field evaporation is aptly named the image hump model, which describes field evaporation as a thermally assisted probabilistic process. Hereby, the probability of field evaporation P_{evap} can be described using the Maxwell-Boltzmann equation [7]

$$P_{\text{evap}} \propto \exp \left(-\frac{Q(F)}{k_B T} \right), \quad (2.1)$$

which is both influenced by the temperature T and an energy barrier $Q(F)$ depending on the local applied electric field F . In this equation, k_B is the Boltzmann constant. The energy barrier and its dependence on the electric field is visualized in Figure 2.1, where the potential energy diagrams are drawn as a function of the distance x to the sample surface for the atom and the ion with and without an external electric field. In the absence of an external electric field, the potential energy of a surface atom can be approximately described by a Lennard-Jones potential [16]. The energy required to free this atom from the surface, equal to the depth of the potential well, is denoted by the sublimation energy

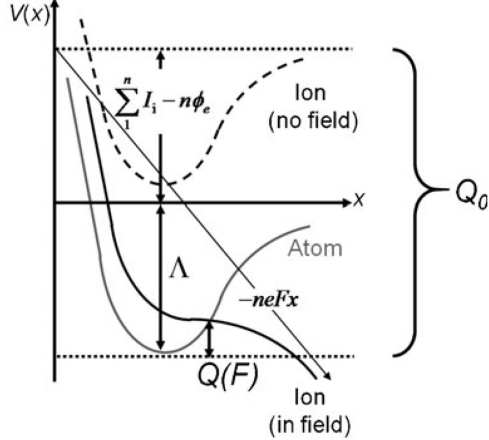


Figure 2.1: The potential energy diagram for an atom and an ion as a function of distance to the surface x , with and without an external electric field. Λ is the sublimation energy, V is the potential energy, n is the degree of ionisation, e is the charge of an electron, I_i is the i th ionisation energy and ϕ_e is the electron work function. The energy barrier with and without an electric field are represented by $Q(F)$ and Q_0 , respectively. Image taken from [7].

Λ . For an atom in the ionic state, this potential energy curve shifts up by the sum of the ionization energy required to form the n -fold charged state from the neutral atom $\sum_1^n I_i$, corrected for the energy gained due to the transfer of n electrons to the surface $n\phi_e$. Here, ϕ_e is the electron work function. The energy Q_0 required to remove the atom from the surface of the sample in the absence of an external electric field is given by [7]

$$Q_0 = \Lambda + \sum_1^n I_i - n\phi_e. \quad (2.2)$$

In the image hump model, under an external electric field F , the potential of the ionic state deforms due to the interplay between an attractive and a repulsive force, attributed to the electrostatic image force and the coulomb force, respectively [17]. Consequently, the energy barrier as a function of electric field $Q(F)$ can be written as:

$$Q(F) = Q_0 - \sqrt{\frac{n^3 e^3}{4\pi\epsilon_0} F}, \quad (2.3)$$

where ϵ_0 is the dielectric permittivity of the vacuum. The field for which this energy barrier is reduced to zero is called the evaporation field.

During an APT measurement, several charge states of the same element can be found. In the image hump model, it is assumed that the atom is fully ionized before escaping from the surface. However, due to the high electric fields, post-ionisation of the formed ion can occur. This process is field dependent [7] and, therefore, it could be used as a measure of the local electric field. To this end, the charge-state-ratio (CSR) can be used, which is defined as the ratio between the number of detected ions from the same elemental species but with different charge states. In this work, it is defined as the ratio between the number of silicon ions with a 2-fold and a single charged state. A high CSR is an indication for a high electric field.

For most materials, the match between the predictions of the image hump model and the experimental findings is generally poor [17]. However, this comprehensible model is suitable to create an intuitive picture of field evaporation.

2.2 Atom probe setup

As previously described, an atom probe measurement relies on the controlled field evaporation of the atoms located on the surface of a needle-shaped sample. A schematic depiction of a local electrode atom probe (LEAP) setup is provided in Figure 2.2. Here, the controlled evaporation of the sample is achieved by applying a DC bias between the needle-shaped sample and a local electrode. Due to the sharp tip of the sample, this applied bias leads to a large electric field experienced by the surface atoms. Using the description introduced in the previous section, this constant field acts to reduce the potential barrier of field evaporation. However, since the sample is kept at a low temperature (20-70K), it is insufficient to support significant field evaporation. By briefly heating up the tip of the sample using a laser or by applying an additional voltage pulse, the energy barrier can be exceeded. The choice of performing the measurement in voltage or laser pulsed mode is largely based on the conductivity of the sample, which has to be high enough for a voltage pulse to be effective [18]. The energy supplied by the combination of the voltage or laser pulse and the constant electric field is carefully controlled to achieve a desired detection rate, while avoiding evaporation between pulses. An important parameter in the case of voltage pulse mode is the pulse fraction, defined as the ratio between the amplitude of the pulse and the DC bias. After field evaporation, the emerging ions propagate towards a position-sensitive detector.

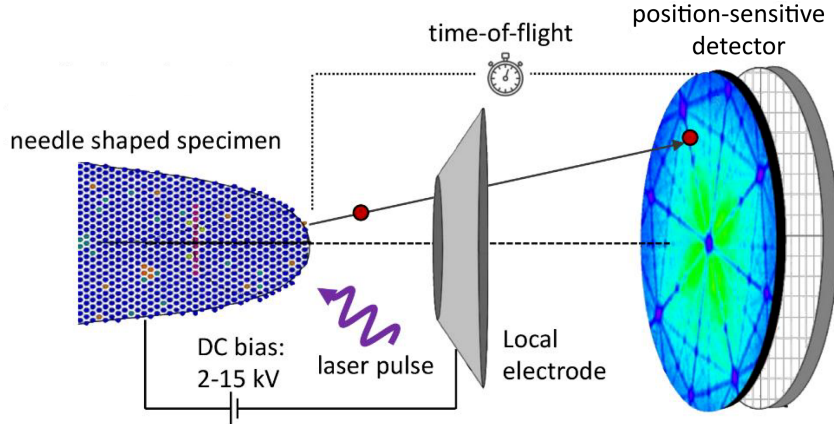


Figure 2.2: A schematic depiction of the local electrode atom probe setup. The needle-shaped specimen, the local electrode and the position-sensitive detector are shown. Image adapted from [19].

A benefit of this pulsed field evaporation is that it provides a known departure time of the ion from the tip's surface. By measuring the time-of-flight (TOF), defined as the time between the pulse and the time at which a hit was registered at the detector, the mass-to-charge ratio can be determined using [7]

$$\frac{m}{n} \approx 2eV \left(\frac{t_f}{L} \right)^2. \quad (2.4)$$

In this equation, e is the electron charge, t_f is the TOF, V is the total voltage and

L is the flight path length. Corrections are made to the TOF to account for voltage variation, the dependence of flight path length on detector location and a time delay induced by the electrical processing [6]. After these corrections, the elemental nature of an ion incident on the detector can be identified. However, not all field evaporated ions lead to a hit registered at the detector, resulting in a limited detection efficiency (DE). The DE is determined by factors such as the open area in the multi-channel plate used in the detector and electronic thresholds [6].

2.3 Samples and sample preparation

As was mentioned in the previous section, samples examined with the APT are needle-shaped in order to achieve the high electric fields required for field evaporation. This requirement leads to tips with a small sidewall angle, tapering to an apex with a diameter between 50 and 150 nm [18]. A low electrical resistance is essential if a voltage mode measurement is desired.

In this work, two distinct sets of specimens are used. The first set comes in the form of a commercially-available grid of 36 presharpened microtips (PSM). These silicon tips are doped to reduce their resistance so that they can be used for voltage mode acquisition. The second set consists of tips containing the SiGe/Si/SiGe multilayer structure. Two types of tips are fabricated out of this multilayer, which differ in the orientation of the top and bottom SiGe layers. In one of these types, the top SiGe is closer to the tip apex with respect to the bottom SiGe layer (top-down preparation), while in the other type the multilayer is rotated 180° such that the bottom layer is closest to the apex (backside preparation). The tips are fabricated starting by removing a wedge-shaped section containing the region of interest (ROI) from a wafer using ion milling and attaching it to a carrier microtip. The structure produced after this step can be seen in the left image in Figure 2.3. A tip is formed out of this chunk by a series of annular milling steps using a focused ion beam (FIB), where the annular pattern is applied with a constant outer diameter and a decreasing inner diameter. As a result of the tip shaping process, gallium atoms can be implanted into the tip and damage may have occurred. Therefore, a low energy cleaning step is implemented to remove the region most affected by gallium implantation. Care must be taken during the tip shaping process to place the ROI at a suitable distance from the tip apex.

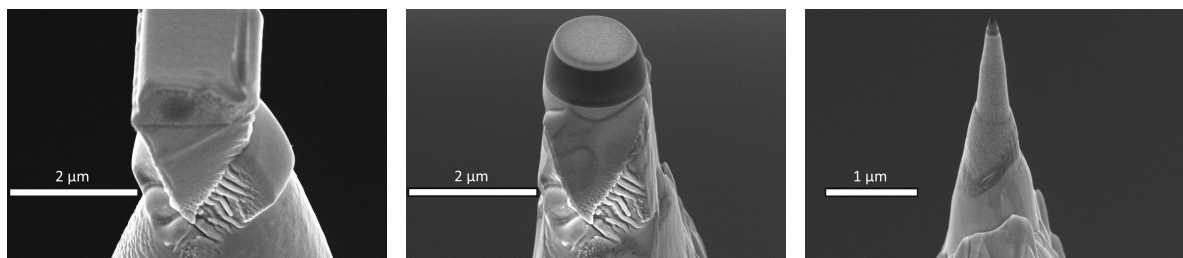


Figure 2.3: SEM images of tip shaping process of the SiGe/Si/SiGe specimen. From the left to the right the tip shaping process is visualized, where in the left image the starting wedge shaped section is shown and on the right image the final tip is presented.

2.4 APT data and reconstruction

The information retrieved after an APT measurement includes the x and y-coordinates of the ion hit positions on the detector, and the TOF of each ion, stored in the order at which the detector hits occurred [6]. This data can be represented in a 2D histogram showing the number of hits per location on the detector. Such a histogram plot is called the detector event histogram (DEH). Some information may already be visible in the DEH, such as low density regions which are related to the crystal structure of the measured material, as will be further explained in Section 4.1. In many cases, however, it is useful to convert this 2D information back to a 3D image of the tip. To this end, a reconstruction procedure needs to be used. Calculating the exact flight path of ions after field evaporation is a complex problem requiring knowledge of the full 3D electric field, from the sample surface to the detector. For example, the local environment of the ion at the surface of the tip is known to drastically influence the ion trajectory [20]. Therefore, simplifying models have been developed to aid during the reconstruction of APT data. The first algorithm proposed in the literature is known as the Bas protocol [21], which, after various improvements, still forms the basis of many commercial software packages [7]. Using a two-step process, this protocol builds the tomographic reconstruction of the analysed volume by determining the depth increment after the lateral positions have been computed. This section briefly describes the Bas protocol and how to tune the required input parameters for the reconstruction.

While formulating the Bas protocol, it is assumed that only the most protruding atoms at the tip's surface are field evaporated as they experience the strongest electric field. As a result, the sample is evaporated layer-by-layer [7]. The sequence of evaporation is therefore indicative of the relative depth of the atoms in the sample. The protocol presumes these layers to be hemispherical. Additionally, the sample is assumed to have a cylindrical shape and the ion trajectories are restricted to lie in a single plane.

Based on these assumption, the lateral coordinates of the reconstruction can be computed using the point-projection model, where ions are modeled to propagate in a straight lines. In reality, it has been calculated that the ion trajectories are initially radial, but are increasingly compressed closer to the detector [7]. The difference between these trajectories is presented in Figure 2.4. In the point-projection model, the real trajectory can approximately be described using a straight trajectory originating from a point P somewhere along the tip axis. The distance between the tip of the sample and P is equal to ξR , where R is the radius of curvature and ξ is the image compression factor (ICF). As the ions follow these diverging trajectories, the image of the tip is effectively magnified as they are projected onto the detector. The magnification M can be written as the ratio between an ion's hit position D to the center of the detector and the distance d between the tip axis and the ion before evaporation. If the detector distance L is much larger than ξR , the magnification can be written as

$$M = \frac{D}{d} \approx \frac{L}{\xi R}. \quad (2.5)$$

A magnification exceeding 10^6 can typically be reached, allowing for the determination of the positions of individual atoms [7]. The hit location on the detector (x_d, y_d) can then easily be linked to a coordinate on the sample surface (x, y) by using:

$$x = \frac{x_d}{M} \text{ and } y = \frac{y_d}{M}. \quad (2.6)$$

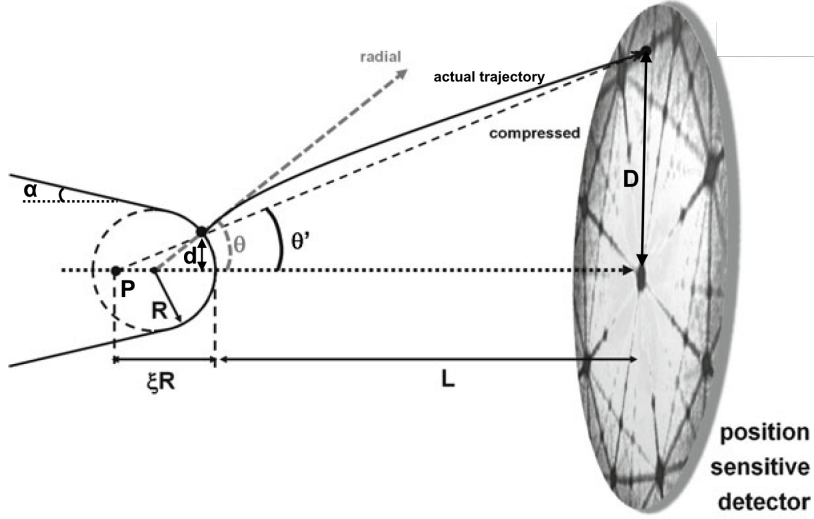


Figure 2.4: A schematic depiction of the point-projection model. The radial, compressed and actual flight paths of the ions evaporated from the sample are shown. The radial and compressed trajectories make an angle of θ and θ' with the specimen axis, respectively. The radius of curvature R , the image compression factor ξ and the detector distance L are indicated, along with the shank angle α and the projection point P . Additionally, the radial distances of a feature to the specimen axis d and the projected feature on the detector D are also labeled. The image is not to scale. Adapted from [7].

As shown in Figure 2.4, the specimen's side walls are tapered by a shank angle α . Consequently, the radius of curvature increases as the sample evaporates. Therefore, the magnification needs to be recalculated for every ion. Three methods exist to determine the radius of curvature as a function of the depth coordinate, which are either based on the applied voltage, a constant shank angle or an image of the sample made prior to the measurement.

The evaporation sequence is used to determine the z coordinate. As the atoms are assumed to be emitted layer-by-layer, the emitting surface of the tip can be incrementally moved by an amount dz . Hence, if the apex of the surface corresponding to the i th ion is at depth z_{tip}^i , then the position of the apex of the following ion can be written as

$$z_{\text{tip}}^{i+1} = z_{\text{tip}}^i + dz. \quad (2.7)$$

Using the TOF data, the ion can be identified and it is assigned a corresponding atomic volume Ω_i . Taking into account the limited detection efficiency μ , the analysed volume can be calculated as the sum over all evaporated atomic volumes. Alternatively, the analyzed volume can directly be calculated from the geometry of the sample. By equating the resulting analyzed volume to the one obtained by summing the atomic volumes, the depth increment can be computed using

$$dz = \frac{\Omega}{\mu w_v(z)}, \quad (2.8)$$

where Ω is the average atom volume and $w(z)$ describes the increase in the analysed volume as a function of the depth coordinate. In the Bas protocol, $w(z)$ is taken to be equal to the analyzed area S_a , which can be computed using $S_a = S_d/M^2$. Here, S_d the surface area of the detector. The z-coordinate calculated in this way is corrected to take into account the assumed spherical emitting surface.

In contrast to the straight flight path instrument described in this section, the setup used to perform the measurements in this work has a reflectron to increase the mass resolution. This complicates the reconstruction protocol by inducing a deformation in the ion trajectories. In commercially available instruments, this deformation is accounted and corrected for, prior to the reconstruction [7].

2.5 Artefacts and corrections

Due to the underlying assumptions made during the formulation of the previously described reconstruction protocol, artifacts can be introduced into the reconstructed volume. For example, the magnification is assumed to only depend on global geometric parameters, neglecting the presence of precipitates or layers with different evaporation fields [8]. In the case of multilayer specimens, this results in the creation of artificial high and low-density regions and a curvature in the interfaces present in the reconstructed volume [22]. These unexpected variations can be attributed to the so-called local magnification effect, which is related to a deviation of the assumed spherical tip shape, and to the alternation from the expected evaporation sequence as assumed in the Bas protocol [9, 22]. The severity of this artifact is dependent on the dissimilarity between the evaporation fields of the layers, where a difference exceeding 10% is expected to yield strong density fluctuations [8]. A direct consequence is the dependence of the reconstruction on the analysis direction [23] and an artificial compression or elongation of the interfaces [13]. Therefore, if it is desired to characterise the interfaces using APT, a correction may need to be applied. A simple density correction has been proposed which is based on the evaporation order of the ions in a small ROI chosen such that it has small lateral dimensions and that top and bottom interface lie sufficiently far away from the interfaces [8]. The position z^i of the i th evaporated ion in the ROI is then linearly redistributed using

$$z^i = z_{\min} + (z_{\max} - z_{\min}) \cdot \frac{i}{N}. \quad (2.9)$$

In this equation, N is the number of ions in the ROI, and z_{\min} and z_{\max} are the minimum and maximum z-coordinates of the first and last ions, respectively. A downside of this density correction is the slight degradation of the depth spatial resolution.

Additional corrections exist to rectify the artifacts found while reconstructing a 3D image of the specimen from APT data [24]. By applying a more complex reconstruction method, the creation of these artifacts may even be avoided. However, these methods often rely on the calculation of the complex electric field lines dictating the ion trajectories [25, 26], the presence of clear crystallographic information [27, 28], or the knowledge of the dynamics of certain reconstruction parameters [29]. Therefore, in this work, only the effect of density correction will be examined.

3 | Data analysis

This chapter will describe the process of obtaining the desired information relevant to this work from the APT data. The data is acquired using a LEAP-5000XR, either in voltage or laser pulse mode. The first section will describe the initial steps taken towards making a 3D reconstruction from the 2D APT data retrieved after a measurement. A few methods to calibrate the reconstruction are also proposed. After the reconstruction, various parameters can be obtained in order to characterize the SiGe/Si interfaces. This will be described in Section 3.2.

3.1 Application of the reconstruction protocol

The commercial software IVAS 3.8.10 is used to reconstruct a 3D image of the specimen. In this software, the reconstruction is performed step-by-step. In the first steps, the region of interest (ROI) is selected. Only the ion hits fitting in the selected region will be used during the further reconstruction. Hereafter, in the next step, the corrections are applied to the TOF spectrum, as explained in Section 2.2. This is followed by a calibration of the mass spectrum by identifying peaks and applying a shift such that these peaks are on their expected locations. Subsequently, the peaks in the mass spectrum can be identified and the proper atomic species or molecular entity can be assigned. The resulting spectrum for a SiGe/Si/SiGe specimen can be seen in Figure 3.1, where a number of peaks in the spectrum are labeled. The red and gray bands indicate the Si and Ge peaks. In the final step, the reconstruction of the data is done.

Setting up the reconstruction begins with selecting the method of radius revolution of the tip. As previously described in Section 2.4, three methods can be chosen for this purpose. In the voltage method, the radius is calculated based on the applied voltage at the time of the evaporation, a constant depending on the geometric considerations and the evaporation field [6]. This method relies on multiple parameters to be provided by the user, which may not be straightforward to define. The second method uses a constant shank angle and the initial tip radius to determine the radius evolution. For the third method, a SEM image of the tip is required and using profile-tracers, the radius at different depths along the z-axis can be determined. Care must be taken in placing the top most profile-tracer at the radius at which the acquisition started. In the case that the sample has a constant shank angle, these last two methods are equivalent. In this work, a SEM image made prior to the measurement is used to determine the tip profile.

After this, only four parameters need to be defined: the (x,y)-coordinates of the reconstruction centre, the image compression factor (ICF) and the detection efficiency (DE). Setting the reconstruction centre has the effect of tilting the reconstruction [6]. A proper choice is to set the coordinates such that the reconstruction centre correspond to a pole location, the reason of which will be explained in the following chapter. Tuning the ICF

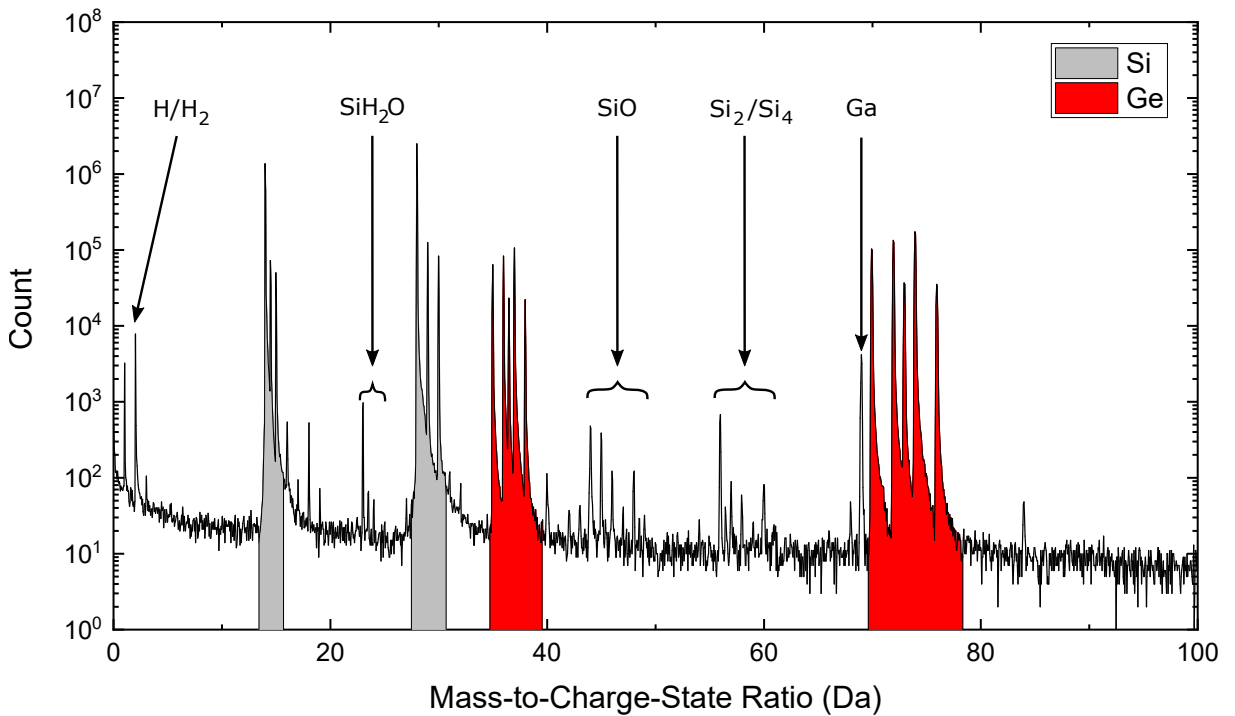


Figure 3.1: The mass-to-charge-state ratio of the SiGe/Si/SiGe multilayer specimen. A number of peaks are labeled. The red and gray bands indicate the Si and Ge peaks.

and the DE is less straight forward. It is known that the ICF will be between 1 and 2, corresponding to a radial and stereographic projection, respectively [7]. The DE is a system specific number, which is expected to be about 52% for the LEAP-5000XR.

With these restrictions on the ICF and the DE in mind, the exact values can be tuned based on geometrical considerations. If the measurement did not result in a fracture, a SEM image before and after the measurement can be used to determine the depth to which the sample has evaporated. Additionally, the radius of curvature measured at the bottom and top surfaces of the reconstructed volume can be determined from the SEM images, which should be matched by the radius of curvature found in the reconstruction, provided that the entire ion sequence is considered during the reconstruction. As multiple measurements on the SiGe/Si/SiGe samples resulted in a fracture, no SEM image could be obtained after the measurement, meaning these parameters could not be used. However, since the thickness of the Si layer is known through complementary measurements such as cross section TEM 1.1 and the SiGe/Si interfaces are expected to be mostly flat due to the controlled epitaxial growth, these parameters could be used to aid during the reconstruction. Furthermore, it is well known that both Si and Ge have a diamond lattice structure [30], which could possibly be used to calibrate the reconstruction. An evaluation is provided whether the crystal structure can be utilized during the reconstruction in the following chapter.

3.2 Interface characterisation

After the tomographic reconstruction, the parameters of interest for the characterisation of the interfaces can be extracted. In this work, the transition width and the RMS and mean roughness of the SiGe/Si interfaces are determined. The transition width is found by defining a $10 \times 10 \times 30$ nm cubical ROI centered around the reconstruction center. This smaller ROI is taken because a slight curvature of the SiGe/Si interfaces may be present

after the reconstruction, which influences the interface characterisation. The center of the ROI is set to the reconstruction center so that the interfaces are perpendicular to the axis along which the profile is calculated. A concentration profile can then be created showing the transitions between the SiGe layers and the Si well, as shown in Figure 3.2a. Hereafter, the transition width can be determined by fitting a sigmoidal function $f(z)$ as a function of the position in the evaporation direction z following [13]

$$f(z) = \frac{C}{1 + \exp\left(-\frac{z_0 \pm z}{\tau}\right)} + V, \quad (3.1)$$

where C is a scaling parameter, and z_0 and V are the horizontal and vertical positioning parameters, respectively. The sign before z corresponds either to an increasing or decreasing function. The transition width is then given by 4τ , which represents the distance of the points where the graph is approximately at 12% and 88% between the horizontal asymptote.

The rms and mean roughness are determined by creating an isosurface where the concentration of Ge is 15 at%. This is done for the default voxel size of 1x1x1 nm and a delocalization of 3x3x1.5 nm. The delocalization acts to prevent the introduction of artifacts formed by binning the position of the ions in the reconstructed volume [31]. A visualisation of the found isosurfaces in the ROI is provided in Figure 3.2b. These isosurfaces are then imported into Gwyddion, which can calculate the rms and mean roughness [32].

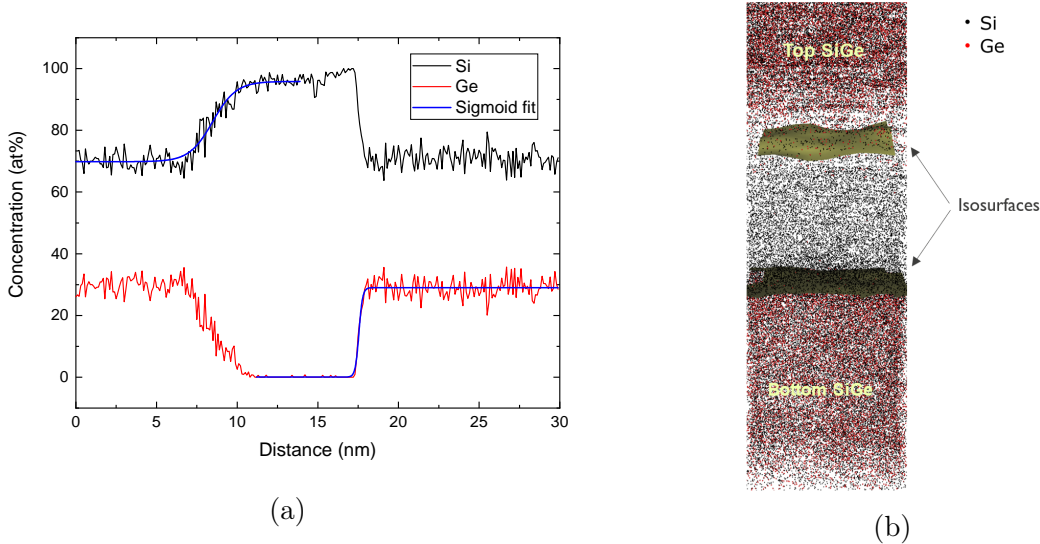


Figure 3.2: (a) A concentration profile as a function of distance from the top of the ROI. Examples of the sigmoidal fits are provided in blue. (b) A visualisation of the isosurfaces (in yellow) created at 15 at% Ge.

4 | Crystallography for reconstruction calibration

Crystallographic information is present in APT data in the form of density fluctuations in the detector event histogram (DEH), and through the formation of crystallographic planes in the 3D reconstruction [33]. This information can be used to calibrate the ICF and the DE in the currently used reconstruction protocol [34], or it can form the basis for a crystal-mediated reconstruction [27, 28]. Additionally, an existing reconstruction can be corrected by identifying the theoretical crystal positions and shifting the reconstructed atoms to these positions [35]. In this case, it will be investigated if the crystallographic information can be used to calibrate the reconstruction parameters in IVAS for the case of SiGe/Si/SiGe multilayers. First, a short description of the origin of crystallographic information in APT data and how it can aid during the reconstruction will be provided. Hereafter, the usability of the crystallographic information in the acquired data is assessed for various performed measurements. A filtering method is applied to enhance the crystallographic features visible in the APT data. As a preparation for the multilayer, a presharpened silicon microtips (PSM) tip is examined as it is expected to more clearly show the crystallographic features, since the introduction of interfaces within the tip may disturb the controlled layer-by-layer evaporation. After this, the filtering method is applied to the multilayer.

4.1 Crystallography in APT data

A typical example of a DEH obtained from a measurement on a PSM can be seen in the left image of Figure 4.1. A characteristic cross of low-density lines can be distinguished, called zone lines. At the crossing between these two zone lines, a pole is located, corresponding to a specific crystallographic direction [7]. For amorphous materials, no high or low density regions in the DEH would be expected. However, the silicon tips possess a diamond lattice structure and are grown in the $<100>$ direction. As a result, the evaporation does not occur homogeneously across the specimen's surface. More specifically, the specimen's apex is approximated to be hemispherical throughout the measurement. Accommodating the cubic lattice to this spherical surface leads to the formation of surface terraces and concentric rings. In the right image in Figure 4.1, the most protruding atoms at the specimen's surface are shown for a tip with a diameter of 54.3 nm. The concentric rings are formed where the spherical surface cuts through crystal planes, the centers of which correspond to poles that may be visible in the DEH. Here, only the $<100>$ pole can directly be resolved. The formation of edges and terraces leads to local variations of the number of neighbors and with that the evaporation field. Additionally, the specific surface topology leads to regions of relatively high and low electric fields, where the electric field in a pole is increased related to the small terrace size [36]. The majority of

the evaporation events will occur at the edges where the atoms have a lower evaporation field and experience a relatively high electric field [37].

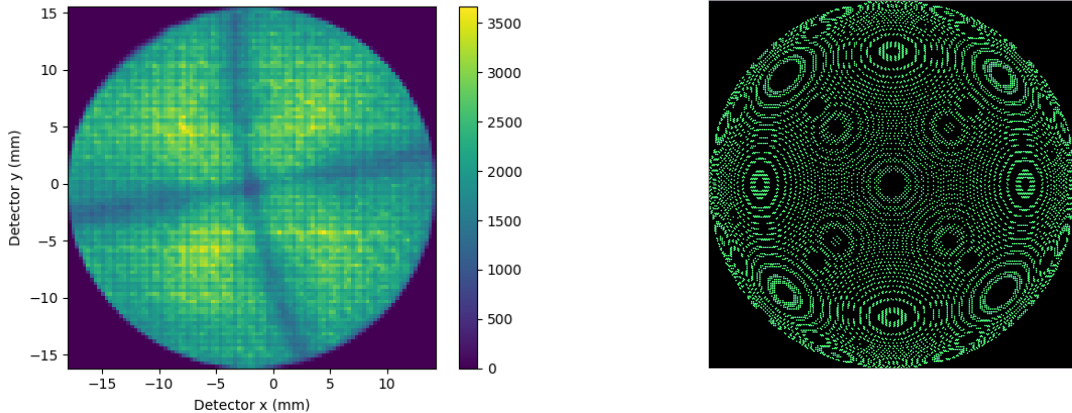


Figure 4.1: In the left image, the detector event histogram is shown for a PSM measured in voltage mode with a pulse fraction of 0.2, a detection rate of 0.2% and a base temperature of 50 K. The color-bar indicates the number of hits in that location. In the right image, a projection is shown of a hemispherical cap with a diameter of 54.3 nm intersecting the diamond crystal structure.

Comparing the two images in Figure 4.1, the 4-fold symmetry around the $\langle 100 \rangle$ pole can clearly be observed. However, a simulation of the exact structures found in the DEH is not trivial. It comprises of the calculation of the trajectory of the ions from the specimen's surface towards the detector. It has been established that local variations at the specimen's surface lead to aberrations in the ion trajectories [20, 28, 36, 37], complicating the calculations. Nevertheless, the pattern formed on the DEH is closely related to the stereographic projection of the crystal structure [36], leading to the possibility to identify the poles and zone lines. With all poles identified, the orientation of the crystal structure with respect to the lab's reference frame can be uncovered [7]. More importantly for this work, the structures can then be used to calibrate the reconstruction parameters [34]. The ICF ξ , for instance, can be approximated by comparing the angle θ_{crys} between two theoretical crystallographic directions to the angle θ_{obs} observed between the corresponding poles on the DEH using

$$\xi \approx \frac{\theta_{\text{crys}}}{\theta_{\text{obs}}}. \quad (4.1)$$

As was previously mentioned, additional crystallographic information is uncovered after the 3D reconstruction of the specimen's volume through the formation of crystal planes. If a pole has been identified, the theoretical plane spacing can be compared to the observed spacing in the reconstruction. Visualisation of the planar spacing can be done using spatial distribution maps (SDMs). An SDM is constructed by appointing a reference atom and drawing vectors to the surrounding neighbors. This process is repeated for each atom in the data set as reference atom [6]. The resulting vectors can be displayed in a 1D distribution showing the offset between the atoms relative to the reference atoms in a specified direction, or as a 2D histogram representing the average distribution of atoms in a certain plane. In a 1D-SDM aligned perpendicular to the crystal planes, the plane spacing can be determined as the distance between two consecutive maxima. Both the ICF and the DE have an influence on the plane spacing and using the 1D-SDM, both of

these parameters need to be tuned to form the optimal reconstruction. Additionally, as explained in Section 3.1, while using the profile-tracers to determine the radius revolution, the placement of the uppermost profile-tracer is crucial for the resulting reconstruction.

4.2 Retrieving crystallographic information

In general, crystallographic information is best recovered for conductive specimens measured in voltage pulse mode at low temperatures, as the controlled evaporation of the specimen is crucial for the visibility of these features [36]. In these cases, the approximation of the layer-by-layer evaporation made during the formulation of the reconstruction method is most appropriate. However, the materials examined during this work are semiconductors and, thus, some of the crystallographic information might not be readily visible. In order to assess if the crystal structure can be used in the case of SiGe/Si/SiGe multilayers, the obtained data needs to be further analyzed. Multiple methods have been proposed in the literature to retrieve crystallographic information from APT data [36, 38–40]. Notably, it has been shown that filtering the DEH for the number of pulses before an evaporation event reveals the location of previously obscured poles for Al and Fe-15at% Cr specimens [41]. This behavior is related to the probability of field evaporation of the atoms on the tip’s surface. In the case the applied electric field F is close to the evaporation field F_e and the temperature is constant, Equation 2.1 can be rewritten to find the mean time required for evaporation τ , such that [40]

$$\tau \propto \exp\left(-a \frac{F - F_e}{F_e}\right). \quad (4.2)$$

In this equation, a is a constant depending on temperature and the energy barrier in absence of an electric field. Since the evaporation field is only reached during the pulses and the detection rate is set low enough to decrease the chance of multiple detector hits per pulse, the time between evaporation events is proportional to the number of pulses. Simulations have shown that atoms laying on low index poles are subjected to a higher electric field, while having a lower evaporation field [37]. This leads to a lower number of pulses required to evaporate these atoms compared to those originating from outside these features. In Section 2.1, the evaporation was presumed to be a thermally assisted process. If there were no local variations in the electric and evaporation fields, this would imply that atoms are picked randomly from the surface of the tip and that the location of subsequent hits on the detector are independent. It has previously been experimentally observed that some consecutive events are in fact spatially and temporally correlated, which is suggested to be linked to the crystallographic structure of the analyzed surface [40].

Here, it is investigated if this method can reveal additional information in the measured semiconductor samples. As an initial verification, the data of a doped silicon PSM is analyzed. This data is acquired in voltage mode with a pulse fraction of 0.2, a detection rate of 0.2% and a base temperature of 50 K. First, the data is compared to the case in which there are no local electric and evaporation field deviations in order to confirm if the crystallographic structure could have influenced the measurement. The results of this analysis are presented in Figure 4.2. In the left plot of Figure 4.2, a histogram is plotted of the number of pulses N_p between two consecutive hits on the detector. The red line indicates the theoretical prediction if the evaporation was a Poisson process, for which the probability of evaporation after N_p pulses is given by [40]

$$P(N_p) = D \exp(-N_p D), \quad (4.3)$$

where D is the detection rate. The detection rate is corrected for the size of the ROI by calculating the average number of pulses between two events, which is about 530 pulses. Sizeable deviations can be seen between the histogram and the theoretical prediction. At low values of N_p , the difference is particularly large, indicating that the consecutive hits follow in a quick succession and that these evaporation events are correlated in time. Moreover, if a histogram is made of the hit distance on the detector for the pulses between which $N_p < 10$, it is clear the hit positions are closely spaced. If it was a pure stochastic process, the histogram will show a distribution centered around the radius of the circular ROI, which is 15 mm in this analysis. This means the events are also correlated in space and that filtering for the number of pulses could reveal pole locations in the DEH.

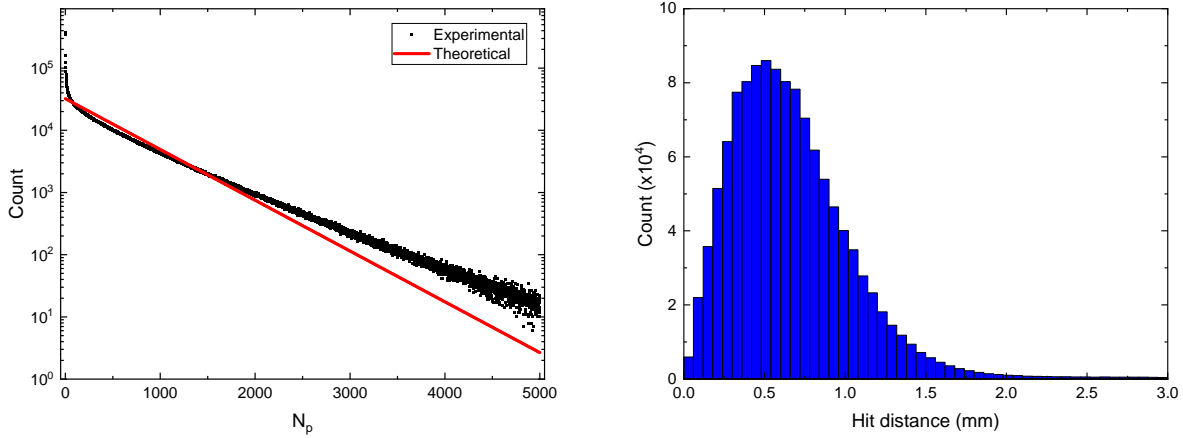


Figure 4.2: In the left plot, the experimental histogram of the number of pulses N_p is shown in black, along with the theoretical prediction following a Poisson process visible in red. In the right plot, a histogram is shown with the distance between consecutive hits between which $N_p < 10$. The experimental findings are based on a voltage mode measurement of a PSM, with a pulse fraction of 0.2, a detection rate of 0.2% and a base temperature of 50 K.

In the left image in Figure 4.3, the unfiltered DEH is shown of the silicon PSM. The centre $\langle 100 \rangle$ pole is already visible, along with a cross made out of zone lines. On the right image, the DEH is filtered for the events where $N_p < 10$. This interval is chosen to maximize the visibility of the pole structure in the DEH. The zone lines can be seen to have narrowed and some additional features seem to appear. However, no new poles have clearly emerged. This is possibly due to the high number of hits outside of the pole locations, meaning that due to the statistical nature of field evaporation, the number of hits of which the $N_p < 10$ is also high. One way to resolve this, is to colorize a histogram bin at a location (x, y) based on the average number of pulses $N_{p,\text{av}}$ that have occurred before the hits at that location, as suggested in [41]. To this end, the number of pulses occurring between the hit at (x, y) and the previous hit elsewhere on the detector is computed $N_{p,n}(x, y)$, for every hit n on the detector. Omitting the indication of the coordinate, $N_{p,\text{av}}$ can be computed using

$$N_{p,\text{av}} = \frac{\sum_{n=1}^{N_{\text{hits}}} N_{p,n}}{N_{\text{hits}}}, \quad (4.4)$$

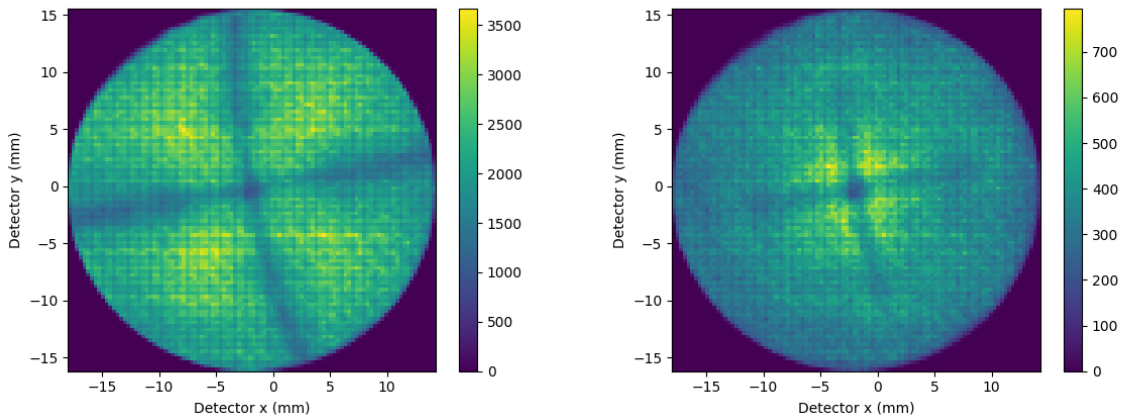


Figure 4.3: In the left image, the detector event histogram is shown for a PSM measured in voltage mode with a pulse fraction of 0.2, a detection rate of 0.2% and a base temperature of 50 K. In the right image, this histogram is filtered for hits before which the number of pulses was smaller than 10.

where N_{hits} is the total number of hits at location (x, y) . The result of this extra step on the DEH can be seen in the left plot in Figure 4.4. Here, a total of five poles are uncovered in the DEH, visible as local minima in the average number of pulses required before an evaporation. Alternatively, a bin can be colorized by normalizing the number of hits at a location $N_{\text{filter}}(x, y)$ after the filtering for $N_P < 10$ with the number of hits prior to the filtering, such that

$$N_{P,\text{norm}} = \frac{N_{\text{filter}}}{N_{\text{hits}}}. \quad (4.5)$$

The result of this filter is shown in the right plot in Figure 4.4. Next to the previously uncovered poles, some extra features seem to have emerged. To the author's knowledge, this is the first time this pattern has been uncovered. For now, the origin of these features is unknown. A detailed simulation, such as presented in [42], might give additional insights into the formation of these patterns. These simulations are outside of the scope of this work.

Comparing the plots in Figure 4.4 to the stereographic projection of silicon, it is expected that the outside structures correspond to the $\langle 311 \rangle$ poles, which is confirmed by previous works [7, 35]. To test whether the local electric field was indeed higher at these pole locations, the CSR could be examined, since a higher field results in a higher probability of post-field ionization. However, in the case of a voltage mode it is observed that the vast majority of the Si ions in the mass spectrum have a $2+$ charge, meaning that the CSR is close to one. Now, having identified five poles, Equation 4.1 could be used to calculate the ICF. However, the use of a reflectron in the atom probe setup complicates the computation of θ_{obs} and, therefore, this equation cannot directly be applied. Instead, if these structures correspond to the mentioned poles, the theoretical lattice spacing should be recovered in the reconstruction. To this end, the ICF and DE are tuned such that clear peaks are formed in the SDM and that the distance between these peaks, created in a ROI around the center pole, corresponds to the theoretical (400) lattice spacing of 0.136 nm. The values found for the ICF and DE are 1.83 and 37%, respectively. These values depend on the the radius indicated by the top-profile tracer, which is set to 42 nm. The

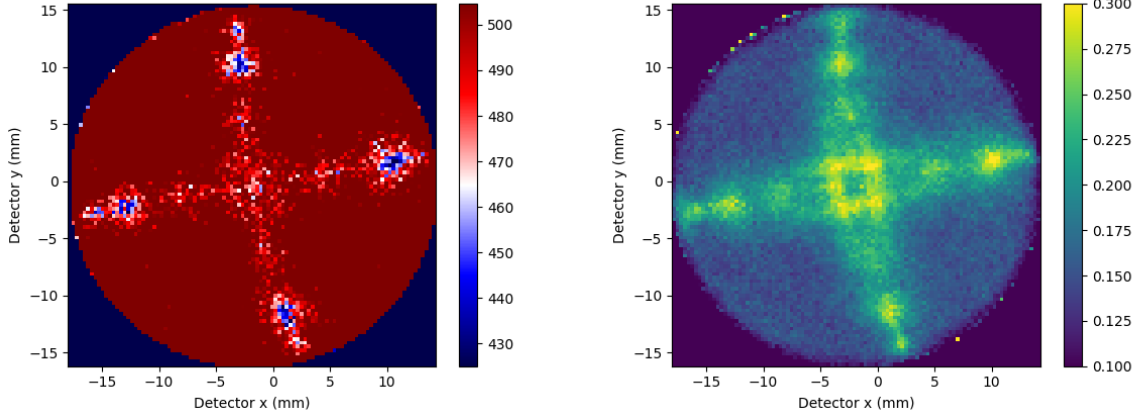


Figure 4.4: Two possible filtering methods to uncover the pole locations. In the left figure, a bin is colorized based on the average number of pulses before an event occurred at that position. On the right figure, the events between which there were less than 10 pulses are computed and normalized by the total number of hits at that position.

resulting lattice spacing at the outside poles should then correspond to the (311) lattice spacing of 0.161 nm. In Figure 4.5, the result of this procedure is shown.

A good correspondence between the theoretical and measured lattice spacing can be seen for the right and bottom pole, which indicates these structures correspond to the $\langle 311 \rangle$ poles. However, no clear periodicity is observed in the left and top pole, where the SDM closely resembles those measured outside the predicted pole locations. This might be attributed to the aberrations caused by the reflectron or other imperfections influencing the reconstruction.

The next step is to test this filtering method on the SiGe/Si/SiGe multilayer samples. As these materials are not doped, the measurement needs to be conducted in laser mode, potentially degrading the crystallographic features in the data. A measurement is conducted on a SiGe/Si/SiGe tip using the lowest possible laser energy (3 pJ). Decreasing the laser energy further increases the required electric field for field evaporation, which leads to a low yield. The ROI is initially taken to encompass all the retrieved data, meaning all the detector hits from the full SiGe/Si/SiGe stack are taken into consideration. From the analysis of the data, the hits on the detector are still expected to be spatially and temporally correlated. This suggests that there may be crystallographic information present in the data.

The resulting DEH and the filtered images can be seen in Figure 4.6. Here, the full reconstructed volume is taken into account. In contrast to the expectations following from the spatial and temporal correlation, no extra poles can be distinguished, even with the additional filtering. Compared to Figure 4.4, there seems to be a field of view change, which could be due to a decrease in the distance between the local electrode and the tip or other unintended experimental differences. Furthermore, the features around the center pole are less clearly defined. This can be related to the heat of the laser pulse influencing the controlled evaporation or to the difference in evaporation fields between Si and Ge. A further distinction between the voltage mode PSM measurement and the measurement conducted on the SiGe/Si/SiGe multilayer is the detection rate, which could also influence the controlled evaporation. In the following, these reasons for the blurring of the crystallographic features are briefly investigated.

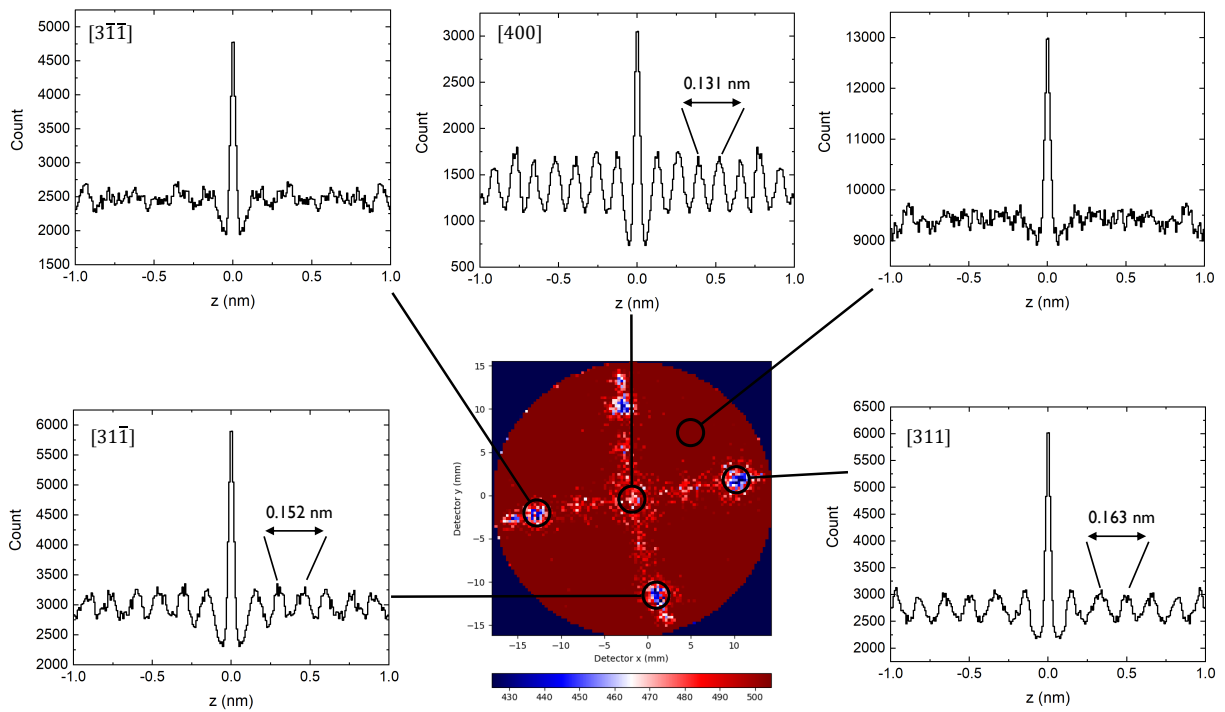


Figure 4.5: The SDM measured in various directions within the ROI. The reconstruction is calibrated based on the lattice spacing of the center pole and the resulting lattice spacing of the outer poles is measured.

First, to investigate the influence of the heat supplied by the laser, a PSM is measured in laser mode with a laser energy of 5 pJ, the result of which can be seen in Figure 4.7. Also here there is a field of view change compared to voltage mode PSM. Even though the features around the pole are faded due to the additional heat of the laser, it cannot fully explain the blurring of these features as seen in the case of SiGe/Si/SiGe. The different evaporation fields between Si and Ge could have a large influence on the blurring of the crystallographic features. A way to avoid this would be to decrease the size of the ROI to lay entirely within the silicon layer. The DEH should then more closely resemble the DEH found from the pure silicon PSM measurements. However, since the proposed filtering method is subject to the statistical behavior of field evaporation, a high number of hits is required ($>$ one million). This cannot be achieved in the thin silicon layer. The influence of the detection rate is not yet known and should be further considered in future works.

With this filtering method, the reconstruction parameters of a PSM measured in voltage mode or at low laser powers can thus be potentially be calibrated. However, an extra correction for the reflectron needs to be added to directly calculate the ICF using Equation 4.1. A downside of this method is that a high number of hits ($>$ one million) is required to properly visualize the crystallographic features in the DEH. Furthermore, the crystallographic features can be seen to blur if the measurement is conducted in laser pulse mode and if the SiGe specimen is used, related to the decrease of the controlled sequential evaporation. Regardless of the spatial and temporal correlation found in the multilayer, no clear crystal planes have been uncovered in the SDM. This means the crystallographic information cannot easily be utilized during the calibration of the reconstruction in this case. The novel filtering method, presented in Equation 4.5, provides a previously undiscovered pattern in the PSM data. The origin and usability of this pattern may be further considered in future works.

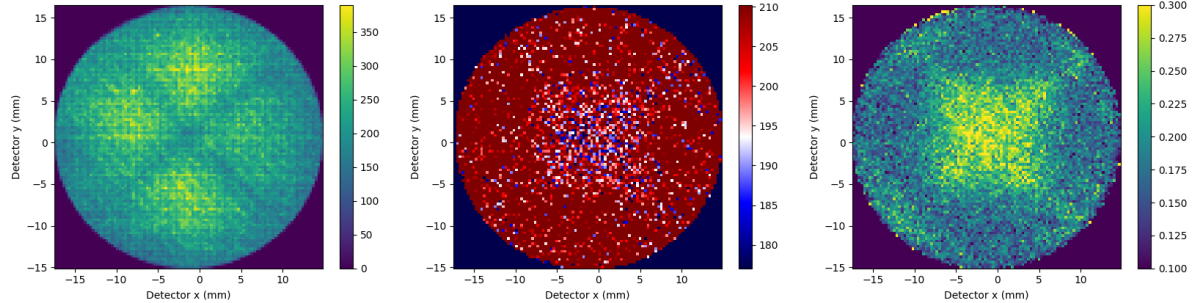


Figure 4.6: In the left image, the DEH of the SiGe/Si/SiGe multilayer is shown acquired with a laser pulse of 3 pJ with a variable frequency and a detection rate of 0.5%. In the middle image, a bin is colorized based on the average number of pulses before an event occurred at that position. On the right figure, the events between which there were less than 10 pulses are computed and normalized by the total number of hits at that position.

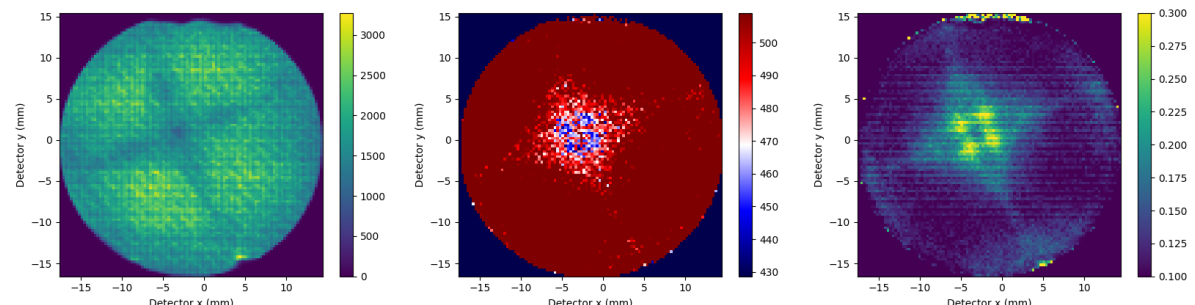


Figure 4.7: In the left image, the DEH of a PSM is shown, which is acquired with a laser pulse of 5 pJ with a variable frequency and a detection rate of 0.2%. In the middle image, a bin is colorized based on the average number of pulses before an event occurred at that position. On the right figure, the events between which there were less than 10 pulses are computed and normalized by the total number of hits at that position.

5 | Influence of density artifacts on interface characterisation

In Section 2.5, it has been discussed that inaccuracies in the tomographic reconstruction can lead to artifacts in the reconstructed volume. One of the expected artifacts in the case of multilayers is the artificial density fluctuations related to a difference in the evaporation fields between the layers. Strong density artifacts are expected to occur if the difference between the evaporation fields exceeds 10% [8]. For Si and Ge the evaporation fields are 33 and 29 V/nm, respectively [43], which means density artifacts could be present in the reconstructed volume. In this chapter, the impact of the density artifacts on the interface characterisation is examined.

Related to the controlled epitaxial growth of the SiGe/Si/SiGe multilayers, it is expected that the roughness and the transition width are close to equal for the top and bottom SiGe/Si interfaces, as defined in Figure 1.1. The density and the concentration of the Si atoms within the reconstructed volume is expected to be constant within the SiGe and Si layers, where the density and the concentration in the Si layer is slightly higher due to the lack of Ge atoms in the lattice. A transition region between the SiGe and the Si layers could be visible. Additionally, the characterisation of the interfaces should be independent of the direction of field evaporation as the tips are formed from the same multilayer sample and, thus, the measurements describe the same interfaces. These expectations are tested against the obtained APT data.

In the left image of Figure 5.1, the TEM image of the used multilayer is again shown. The thickness of the layers is indicated in nm. A specimen is prepared out of this multilayer and measured using a laser power of 30 pJ with a variable frequency and a detection rate of 0.5%. On the right image, the concentration profile as retrieved from the APT reconstruction is displayed. This reconstruction was done as described in Section 3.1, based on the Si layer thickness and the curvature of the SiGe/Si interfaces. The ICF and DE are taken to be 1.65 and 52%, respectively. The initial tip radius is taken to be 50 nm. The layers visible from the concentration profile are labeled and the layer thickness is provided. There are some differences between thickness of the layers in the TEM image and in the concentration profile. This is related to inaccuracies in the reconstruction. Contrary to the expectations, from the concentration profile around the Si layer it can be seen that the top and bottom interfaces are notably different. A relatively sharp transition at the bottom Si/SiGe interface is visible in both the Si and Ge concentrations, while at the top interface this transition is considerably wider. Furthermore, there is a slope in the Si concentration inside the Si layer, where a constant Si concentration is expected.

To examine these discrepancies further, a small cubical ROI of 10x10x30 nm can be taken around the Si layer. The dimensions of this ROI are chosen to avoid the effects of the slight curvature of the layers present in the reconstruction and to capture the complete

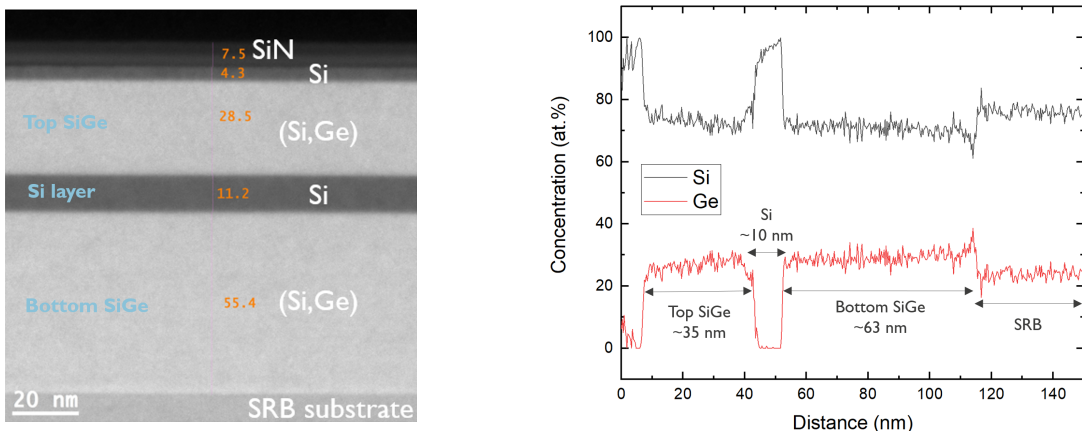


Figure 5.1: A TEM image of the used multilayer is shown on the left. In the right plot, the concentration profile is presented as obtained from the APT reconstruction. In both images, the layers are labeled and the layer thickness is given in nm. This analysis is based on the top-down measurement.

transitions between the layers. After the reconstruction, a projection of the points at which Si and Ge atoms are present in the ROI can be seen in the left image in Figure 5.2a. The normalized Si density as a function of distance from the top of the ROI is provided in the figure. A clear high and low density region are created at the interfaces between SiGe and Si, which correspond to the sharp and wide transition visible in the concentration profile. The slight slope in the concentration profile of Si is created due to the measured increasing Si density accompanied by a relatively constant background of H and H₂ in the Si layer. These hydrogen atoms originate from the residual gas present in the analysis chamber. Related to the higher evaporation field of Si, a higher field is required to maintain a constant detection rate, resulting in an increasing probability of detecting these background atoms during the evaporation of the Si layer. It could be chosen to disregard the hydrogen atoms in future reconstructions, or to correct for the slope by calculating the ratio between the Si concentration and the sum of the Si and Ge concentrations as a function of distance.

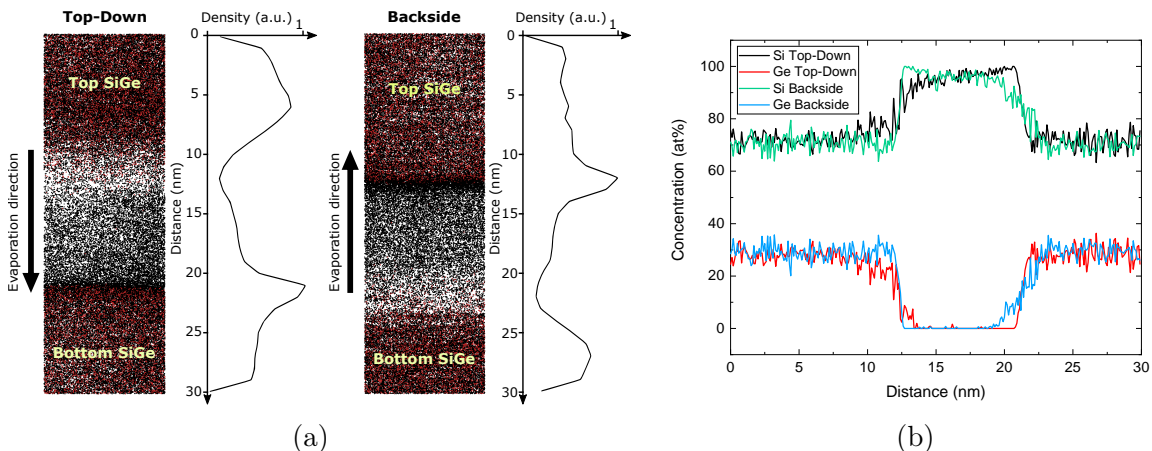


Figure 5.2: (a) A projection of the 3D point cloud as created after the reconstruction for both the top-down and backside evaporation directions. The red and black dots are the Si and Ge positions, respectively. The Si density as a function of distance from the top of the ROI is provided. (b) The concentration profile as a function of distance from the top of the ROI for the top-down and backside evaporation directions.

Thus far, the analysis provided in this chapter has been on a specimen which was field evaporated from the top SiGe towards the bottom SiGe, hereafter referred to as the top-down measurement. As previously explained, the characterisation of the interfaces should ideally be evaporation direction independent. Therefore, in order to confirm if these density fluctuations are a reconstruction artifact, an APT measurement has been preformed where the evaporation direction is reversed. To be able to fairly compare the influence of the evaporation direction, the measurements are performed with the same detection rate and the laser energy is set to get a similar CSR (such that the ions experience a similar electric field). An ICF and DE of 1.65 and 52%, respectively, are used during the reconstruction. The initial tip radius is set to 32 nm. In the reconstruction obtained from this so-called backside measurement, the high and low density interfaces are reversed, as visible in Figure 5.2a. From the concentration profiles, provided in Figure 5.2b, it can be concluded that the transition widths at the top and bottom interfaces are clearly dissimilar between the top-down and backside measurements. The impact of these observed differences on the interface characterisation will be quantified later in this chapter. For now, it can be concluded that these density fluctuations are an artifact of the APT reconstruction and they are not physically present in the specimen.

A method to correct for the density fluctuations has been discussed in Section 2.5. This density correction can be directly applied in IVAS. If DE of 52% is used, the resulting density corrected ROI in both evaporation directions can be seen in Figure 5.3a. The density fluctuation at the interfaces is reduced. Moreover, the concentration profile of Ge for the top-down measurement is now closely matched by the backside measurement. In the Si concentration, there is still a notable slope related to the H and H₂ background and the non-uniform Si density in the Si layer, which depends on the evaporation direction. Due to the density correction, the ROI is slightly elongated and the Si layer appears to be thinner. It has been suggested previously to tune the DE such that the Si thickness closely resembles the actual thickness [13], here provided by the TEM measurement. Furthermore, this change in geometry might influence the values of the parameters found to characterise the interfaces. The extend to which the characterisation parameters are affected by all these dependencies and the used correction will be quantified in the following.

To characterize the interfaces, the rms roughness, mean roughness and the transition width of the Si/SiGe interfaces are computed as explained in Section 3.2. The results are summarized in Figure 5.4. By comparing the top-down and backside measurements, it can be concluded that the roughness and the transition width of the top interface is overestimated by the top-down measurement, while it is underestimated by the backside measurement. The opposite holds for the bottom interface. An overestimation of the parameters at an interface is linked to a low density at that interface, as was also established previously [13]. The deviation between the parameters found by the top-down and backside measurements are substantial, frequently exceeding 300%. The difference is particularly large for the transition width of the top interface computed using the Si concentration profile, where an 8-fold difference is found between the measurements. This is thought to be related to the slope in the Si concentration, where the sigmoidal function assumes a constant concentration. This reduces the validity of using the sigmoidal function to fit this profile and blurs the definition of the 12% to 88% transition. For this reason, the Ge concentration profile will be a better choice to characterize the transition width.

After applying the density correction, the deviation between the parameters in the two evaporation directions is reduced. Therefore, the density correction decreases the depen-

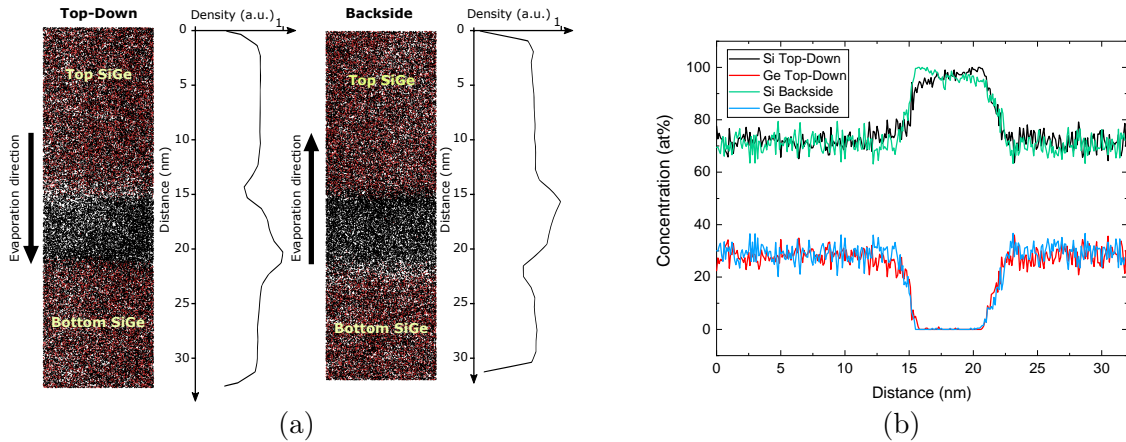


Figure 5.3: (a) A projection of the 3D point cloud as created after the reconstruction and density correction for both the top-down and backside evaporation directions. The red and black dots are the Si and Ge positions, respectively. The Si density as a function of distance from the top of the ROI is provided. (b) The concentration profile as a function of distance from the top of the ROI for the top-down and backside evaporation directions after the density correction.

dence of these parameters on the evaporation direction. By comparing the transition widths acquired from APT data and from scanning transmission electron microscopy (STEM), it has previously been found that only after the density correction the obtained values were in good agreement [13]. However, the values found after the density correction strongly depend on the chosen DE. For example, after performing the density correction with a DE of 37%, it has been found that the transition width increases as the DE reduces. More specifically, the transition width has been found to scale as $1/\text{DE}$. Also the Si layer thickness and the length of the ROI scale in a similar fashion. The exact origin of this dependence is currently unknown and should be further examined in future works.

From this evaluation it can be concluded that, contrary to the expectations, the APT data suggests that the top and bottom interface are substantially different in terms of roughness and transition width. This discrepancy is related to the density artifacts, which depend on the evaporation direction. A density correction has been applied that can decrease the dependence on the evaporation direction and increase the accuracy of the obtained values. The transition width is best determined using the Ge concentration profile, as the slope present in the Si concentration decreases the validity of the sigmoidal fit. Alternatively, a correction could be applied for the slope or the detected hydrogen atoms could be disregarded during the reconstruction. The obtained roughness and transition width parameters are dependent on the choice of the DE used during the density correction, following a $1/\text{DE}$ dependence. The Si layer thickness should be close to the expected thickness to be able to fairly compare the different samples.

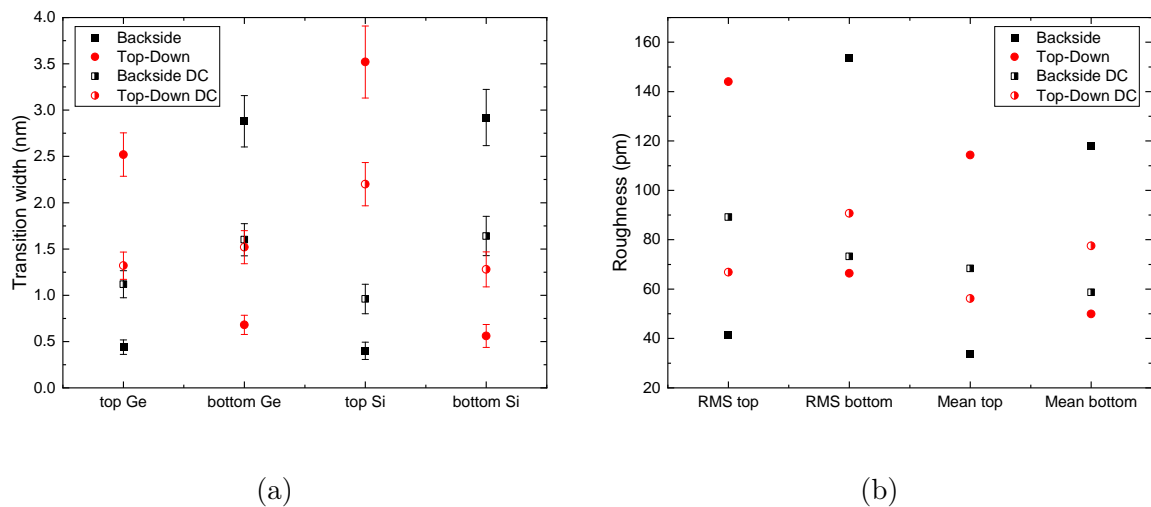


Figure 5.4: (a) The transition width as measured from the Si and Ge concentration profile for the top and bottom interfaces. The error bars denote the fitting error of the sigmoidal function. (b) A plot of the RMS and mean roughness of the the top and bottom interfaces. These parameters are provide for both the top-down and backside measurements, with and without the density correction (DC).

6 | Deviations due to varying the reconstruction parameters

The creation of a tomographic reconstruction from APT data is not a trivial task. As previously discussed in Section 3.1, it requires several reconstruction parameters, which are not straightforward to define. If a SEM image is used to determine the radius revolution, as is done in this work, these parameters include the image compression factor (ICF), detection efficiency (DE), the reconstruction center and the position of the top profile-tracer. Several criteria could potentially be used to guide the choice of these parameters, such as a known layer width, the curvature of interfaces or the spacing between crystallographic planes. Since there is no standardized protocol for choosing the optimal values for these parameters, deviations may be induced in the reconstruction based on the choice of the calibration criteria. An inaccuracy during the calibration could affect the found interface parameters. In this chapter, it is investigated what the impact is of a different choice of these reconstruction parameters on the interface characterisation. For now, only the influence of the ICF is examined.

Several reconstructions have been done with a varying ICF. A similar ROI as described in the previous chapter is used. The change of the interface parameters as a function of the ICF can be seen in Figure 6.1 in case of the top-down measurement. Here, the DE is kept at 52% and the initial radius is fixed at 50 nm. The dependence of the parameters is shown before and after the density correction is applied. Comparing Figures 6.1a and 6.1c, it can be seen that the roughness parameters and the transition width describing the same interface scale in a similar manner. This observation is in line with a previous study in which it was shown that a model using the transition width as input can predict the rms roughness [11]. After the density correction has been applied, the interface parameters corresponding to the top and bottom interface can be seen to shift and become more equal. The magnitude of this shift is dependent on the DE chosen during the density correction, as was also been found in the previous chapter. The interface parameters vary up to almost a factor three if the ICF is changed. A similar dependence on the ICF is observed if the transition width corresponding to the backside measurement is analyzed, as is shown in Figure 6.2. Here, the dependence of the top and bottom interface on the ICF is reversed. There is a slight deviation from this dependence in the roughness parameters, which is found to depend on the reconstruction center.

In Figure 6.3, the reconstructed volume and the ROI can be seen in case an ICF of 1.2 or 1.8 is chosen. The reconstruction is based on the top-down measurement before the density correction is applied. In the case the ICF is 1.2, the top interface shows a strong curvature, while the bottom interface is relatively flat. On the other hand, if an ICF of 1.8 is used, the top interface becomes more flat and the bottom interface shows a stronger curvature. This behavior is reflected by the isosurfaces presented in the figure. This could

explain the dependence of the transition width on the ICF, as a tilt in the interface with respect to the z-axis results in an artificial slope in the concentration profile, broadening the measured transition width. Furthermore, a curvature in the isosurface will result in an increase in the roughness parameters. The choice for the ICF to create a flat interface is, thus, different for the top and bottom interface. Physically, this may be due to out-of-sequence evaporation or alteration of tip shape during evaporation. The reason for the exact dependence of the roughness parameters and the transition width on the ICF is currently unknown and could be further investigated in future works.

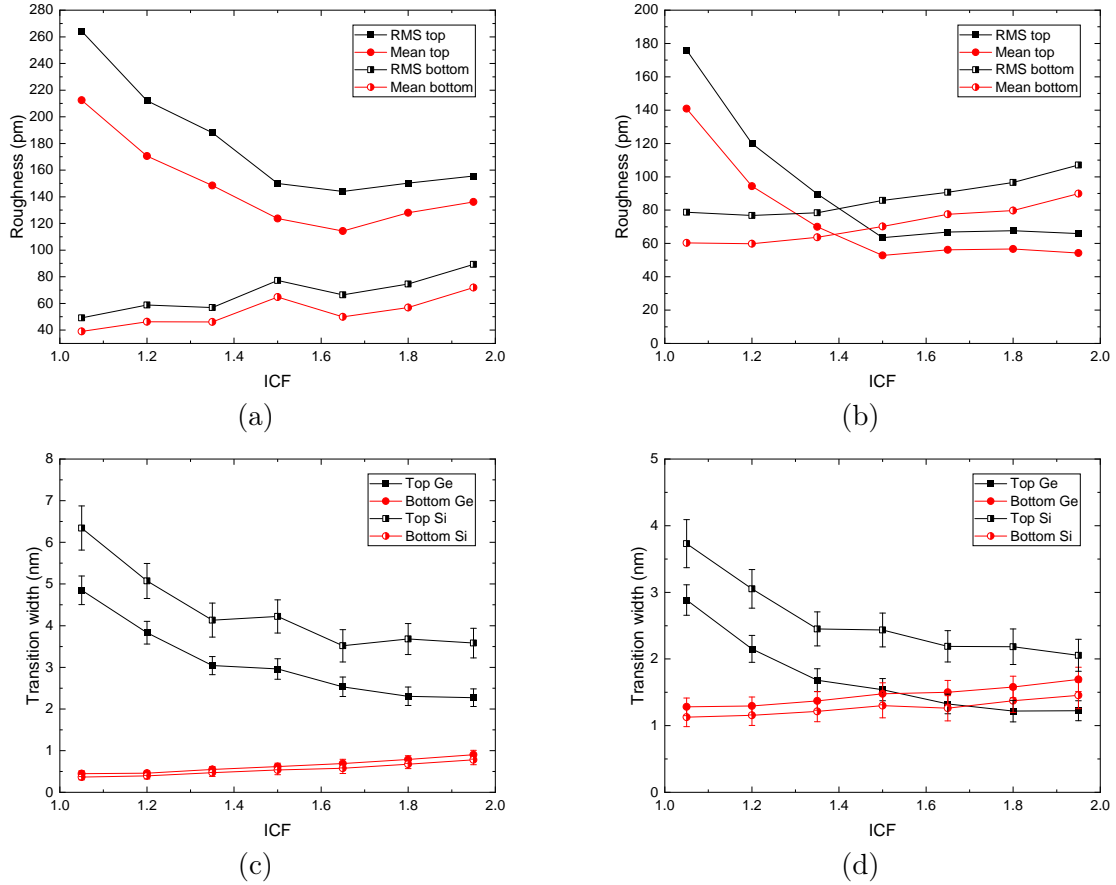


Figure 6.1: In the top plots, the roughness parameters of the top and bottom interfaces as a function of the ICF is presented as found before (a) and after (b) the density correction is applied. In the bottom plots, the transition width at the top and bottom interfaces based on the the Si and Ge density profiles as a function of the ICF is shown, measured before (c) and after (d) the density correction is applied. The error bars indicate the error in the sigmoidal fit.

Next to the interface parameters, the Si layer thickness and the size of the reconstructed volume also scale with the ICF, as depicted in Figure 6.4. The shown dependencies on the ICF can be explained based on the reconstruction protocol described in Section 2.4, from which it is expected that the distances in the z-direction scale with $1/ICF^2$ and the x- and y-dimensions scale linearly with the ICF. The Si layer thickness is decreased up to 30% after applying the density correction, which should be taken into account during the calibration of the reconstruction.

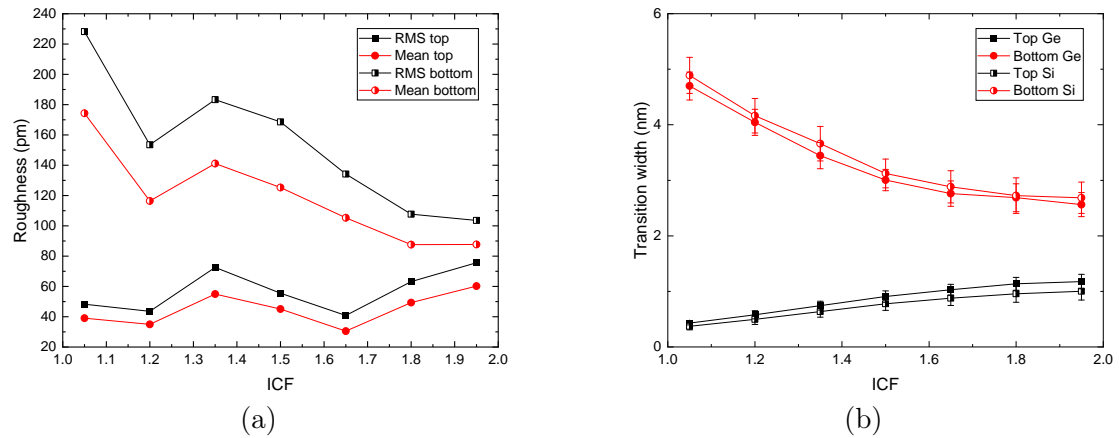


Figure 6.2: (a) The roughness parameters and (b) the transition width as a function of the ICF. The data displayed in the plots is obtained from the backside measurement before the density correction is applied. The error bars indicate the error in the sigmoidal fit.

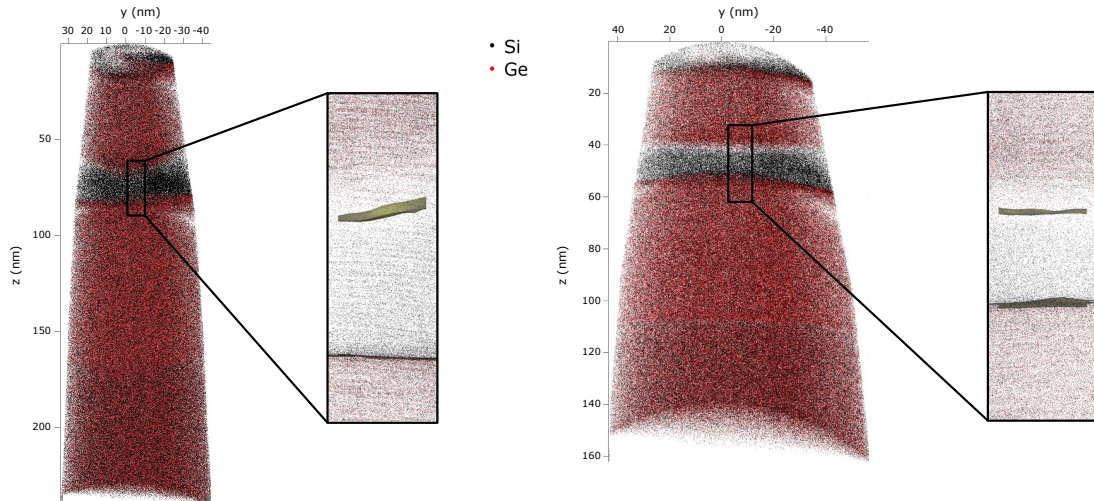


Figure 6.3: The reconstructed volume if an ICF of 1.2 (left image) or 1.8 (right image) is chosen. The cubical ROI is also presented along with the found isosurfaces at 15 at% Ge in yellow. These reconstructions are based on the top-down measurement before the density correction is applied.

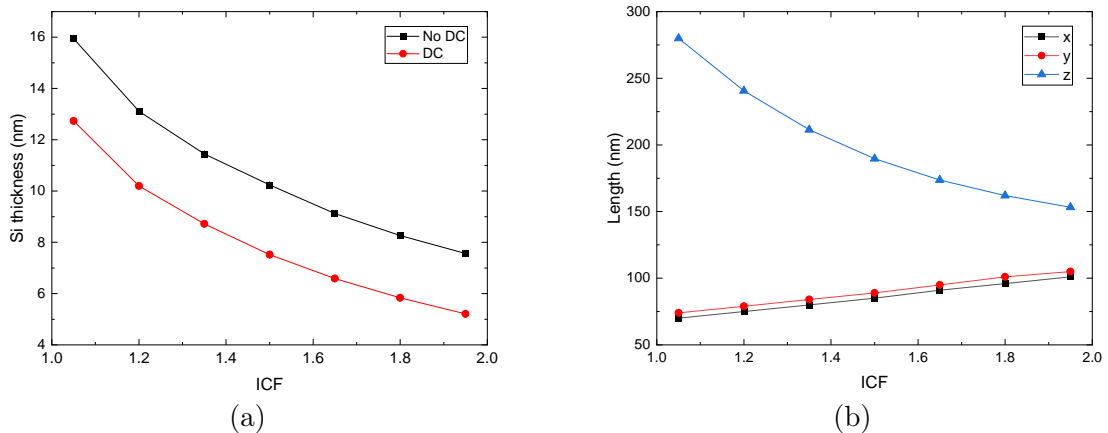


Figure 6.4: (a) The Si layer thickness as a function of the ICF before and after the density correction (DC) is applied. (b) The length of the reconstructed volume in the x, y and z-directions as a function of the ICF before the density correction is applied.

7

Discussion and conclusion

Atom probe tomography is a promising technique to characterize the buried interfaces in SiGe/Si/SiGe multilayers, which show great promise for qubit applications. Using APT, the influence of various fabrication conditions can potentially be mapped and linked to the final qubit performance. However, the artifacts induced during the reconstruction have been shown to impact the interface characterisation. Additionally, the reconstruction parameters can often not unequivocally be determined, leading to further inaccuracies. In this work, the reliability of APT to characterize the interfaces has been examined. In this chapter, a brief overview of the findings presented in this work is provided. Possible directions for future research and a discussion of the results are also given.

It has been attempted to utilize the crystallographic information present in the APT data, with the aim to calibrate the reconstruction parameters. A filtering method has been applied to the DEH of the SiGe/Si/SiGe multilayer which was aimed at uncovering the crystallographic information. Although the filtering method showed great promise when applied to the data of a Si tip, no additional usable information was retrieved in the case of the multilayer specimen. This could be attributed to the laser power and the difference between the evaporation fields of Si and Ge, leading to a reduction in the controlled evaporation sequence. However, the detection rate could also have an influence and should be considered further. To the authors' knowledge, the distinct patterns found in the DEH of the Si tips by the novel filtering method defined in Equation 4.5 have not previously been uncovered. The origin of this pattern could be further investigated in future works.

The influence of the density artifacts and the density correction have been quantified. By measuring the multilayer in two directions, it has been established that the density artifact has a considerable impact on the interface characterisation. The discrepancies between the two measurement directions are mostly alleviated by applying a density correction, motivating the use of this correction in future works. Next to reducing the density fluctuations, it has been found that this correction reduces the apparent Si layer thickness compared to the original reconstruction, which should be taken into account upon interpreting the data. It should be noted that the used density correction is inherently a small field of view correction.

The dependence of the interface characterisation on a change in the ICF has been determined. It has been found that the roughness parameters and the transition width corresponding to the same interfaces scale in a similar fashion with the ICF, both in the case of the top-down and the backside measurements. By varying the ICF between one and two, a deviation of up to three-folds has been found between the minimum and maximum of the interface parameters. The density correction decreases the difference between the parameters found for the top and bottom interface. The aforementioned ICF-dependence is also visible in the isosurfaces. However, obtaining a more quantitative

description could be the topic of future research. It has been found that the ICF for which the least curvature is observed in the interfaces differs between the top and bottom interfaces. Since the electron wavefunction is concentrated near the top interface [11], the ICF could best be chosen based on the top interface. The Si layer thickness and the dimension of the reconstructed volume have been found to scale in a predictable manner.

The rms and mean roughness have been used in this work to characterize the interfaces. These parameters are poor at defining the roughness of curved interfaces. A slight curvature present in the isosurface leads to an artificial increase in these parameters, as they only quantify deviations from a mean line. In this work, this is taken into consideration by using a smaller ROI. This limitation reduces the possibility to characterize larger interfaces and, therefore, could induce a susceptibility to local statistical variations in the interface. Additionally, the creation of the isosurface is dependent on the used delocalization and voxel size. In extension, the roughness parameters are expected to depend on these values as well, which should be further investigated in future works. The values of the transition width have been found by fitting a sigmoidal function to the concentration profiles of Si and Ge created along the z-direction. This method expects the interfaces to lay perpendicular to the z-direction, which may not hold true simultaneously for both top and bottom interfaces. This induces a distortion in the found values. A method to account for this could be to identify the transition width for the top and bottom interfaces separately, setting the reconstruction centre such that the desired interface is perpendicular to the z-axis.

By using the insights provided in this work, potential pitfalls during the reconstruction and the interpretation of the interface parameters can be avoided. The analysis presented in this work is not limited to SiGe/Si/SiGe multilayers and may act as a foundation for similar works on other multilayers examined using APT. In future works, to further determine the accuracy of the interface characterisation, the found parameters could be compared to those obtained from alternative measurement techniques, such as STEM. A more complex reconstruction method could also be examined, which may avoid the assumptions made that resulted in the creation of the described artifacts. For example, a more rigorous reconstruction method could be used based on a bottom-up approach, as presented in [26]. With the acquired insights, the interfaces of SiGe/Si/SiGe multilayers prepared under different annealing conditions can be compared. The differences in the found interface parameters could then be linked to the qubit performance, leading to a set of fabrication conditions to obtain the best performing qubit and paving the way towards unlocking the benefits of the quantum computer.

8 | Bibliography

- [1] A. M. J. Zwerver, T. Krähenmann, T. F. Watson, L. Lampert, H. C. George, R. Pillarisetty, S. A. Bojarski, P. Amin, S. V. Amitonov, J. M. Boter, R. Caudillo, D. Correas-Serrano, J. P. Dehollain, G. Droulers, E. M. Henry, R. Kotlyar, M. Lodari, F. Lüthi, D. J. Michalak, B. K. Mueller, S. Neyens, J. Roberts, N. Samkharadze, G. Zheng, O. K. Zietz, G. Scappucci, M. Veldhorst, L. M. K. Vandersypen, and J. S. Clarke, “Qubits made by advanced semiconductor manufacturing,” *Nature Electronics*, vol. 5, no. 3, pp. 184–190, 3 2022.
- [2] L. M. K. Vandersypen and M. A. Eriksson, “Quantum computing with semiconductor spins,” *Physics Today*, vol. 72, no. 8, pp. 38–45, 8 2019.
- [3] F. A. Zwanenburg, A. S. Dzurak, A. Morello, M. Y. Simmons, L. C. L. Hollenberg, G. Klimeck, S. Rogge, S. N. Coppersmith, and M. A. Eriksson, “Silicon quantum electronics,” *Rev. Mod. Phys.*, vol. 85, no. 3, pp. 961–1019, 7 2013. [Online]. Available: <https://link.aps.org/doi/10.1103/RevModPhys.85.961>
- [4] J. J. Pla, K. Y. Tan, J. P. Dehollain, W. H. Lim, J. J. L. Morton, F. A. Zwanenburg, D. N. Jamieson, A. S. Dzurak, and A. Morello, “High-fidelity readout and control of a nuclear spin qubit in silicon,” *Nature*, vol. 496, no. 7445, pp. 334–338, 4 2013.
- [5] S. Kanai, F. J. Heremans, H. Seo, G. Wolfowicz, C. P. Anderson, S. E. Sullivan, M. Onizhuk, G. Galli, D. D. Awschalom, and H. Ohno, “Generalized scaling of spin qubit coherence in over 12,000 host materials,” *Proceedings of the National Academy of Sciences*, vol. 119, no. 15, p. e2121808119, 2022. [Online]. Available: <https://www.pnas.org/doi/abs/10.1073/pnas.2121808119>
- [6] D. J. Larson, T. J. Prosa, R. M. Ulfig, B. P. Geiser, and T. F. Kelly, *Local Electrode Atom Probe Tomography*. New York, NY: Springer New York, 2013.
- [7] B. Gault, M. P. Moody, J. M. Cairney, and S. P. Ringer, *Atom Probe Microscopy*. New York, NY: Springer New York, 2012, vol. 160.
- [8] F. Vurpillot, D. Larson, and A. Cerezo, “Improvement of multilayer analyses with a three-dimensional atom probe,” *Surface and Interface Analysis*, vol. 36, no. 5-6, pp. 552–558, 2004. [Online]. Available: <https://analyticalsciencejournals.onlinelibrary.wiley.com/doi/abs/10.1002/sia.1697>
- [9] F. Vurpillot, A. Cerezo, D. Blavette, and D. J. Larson, “Modeling Image Distortions in 3DAP,” *Microscopy and Microanalysis*, vol. 10, no. 3, pp. 384–390, 2004.
- [10] N. Madaan, J. Bao, M. Nandasiri, Z. Xu, S. Thevuthasan, and A. Devaraj, “Impact of dynamic specimen shape evolution on the atom probe tomography results of doped epitaxial oxide multilayers: Comparison of experiment and simulation,”

- Applied Physics Letters*, vol. 107, no. 9, p. 91601, 2015. [Online]. Available: <https://doi.org/10.1063/1.4929705>
- [11] B. P. Wuetz, M. P. Losert, S. Koelling, L. E. A. Stehouwer, A. M. J. Zwerver, S. G. J. Philips, M. T. Mkadzik, X. Xue, G. Zheng, M. Lodari, S. V. Amitonov, N. Samkharadze, A. Sammak, L. M. K. Vandersypen, R. Rahman, S. N. Copper-smith, O. Moutanabbir, M. Friesen, and G. Scappucci, “Atomic fluctuations lifting the energy degeneracy in Si/SiGe quantum dots,” 12 2021.
 - [12] S. Koelling, M. Gilbert, J. Goossens, A. Hikavyy, O. Richard, and W. Vandervorst, “High depth resolution analysis of Si/SiGe multilayers with the atom probe,” *Applied Physics Letters*, vol. 95, no. 14, p. 144106, 2009. [Online]. Available: <https://doi.org/10.1063/1.3243461>
 - [13] O. Dyck, D. N. Leonard, L. F. Edge, C. A. Jackson, E. J. Pritchett, P. W. Deelman, and J. D. Poplawsky, “Accurate Quantification of Si/SiGe Interface Profiles via Atom Probe Tomography,” *Advanced Materials Interfaces*, vol. 4, no. 21, p. 1700622, 2017. [Online]. Available: <https://onlinelibrary.wiley.com/doi/abs/10.1002/admi.201700622>
 - [14] E. W. Müller, “Field Desorption,” *Phys. Rev.*, vol. 102, no. 3, pp. 618–624, 5 1956. [Online]. Available: <https://link.aps.org/doi/10.1103/PhysRev.102.618>
 - [15] R. Gomer, “Field Desorption,” *The Journal of Chemical Physics*, vol. 31, no. 2, pp. 341–345, 8 1959.
 - [16] H. Ibach, *Physics of Surfaces and Interfaces*. Springer Berlin Heidelberg, 2006.
 - [17] W. Lefebvre-Ulrikson, F. Vurpillot, and X. Sauvage, *Atom Probe Tomography: Put Theory Into Practice*. Elsevier, 2016.
 - [18] T. F. Kelly and M. K. Miller, “Atom probe tomography,” *Review of Scientific Instruments*, vol. 78, no. 3, p. 031101, 3 2007.
 - [19] M. Dialameh, “Fabrication and characterization of reference nano and micro structures for 3D chemical analysis,” Ph.D. dissertation, Katholieke Universiteit Leuven, Leuven, 2019.
 - [20] A. J. W. Moore, “The simulation of FIM desorption patterns,” *Philosophical Magazine A*, vol. 43, no. 3, pp. 803–814, 1981. [Online]. Available: <https://doi.org/10.1080/01418618108240409>
 - [21] P. Bas, A. Bostel, B. Deconihout, and D. Blavette, “A general protocol for the reconstruction of 3D atom probe data,” *Applied Surface Science*, vol. 87-88, pp. 298–304, 1995. [Online]. Available: <https://www.sciencedirect.com/science/article/pii/0169433294005613>
 - [22] E. A. Marquis, B. P. Geiser, T. J. Prosa, and D. J. Larson, “Evolution of tip shape during field evaporation of complex multilayer structures,” *Journal of Microscopy*, vol. 241, no. 3, pp. 225–233, 3 2011.
 - [23] D. J. Larson, T. J. Prosa, B. P. Geiser, and W. F. Egelhoff, “Effect of analysis direction on the measurement of interfacial mixing in thin metal layers with atom probe tomography,” *Ultramicroscopy*, vol. 111, no. 6, pp. 506–511, 2011. [Online]. Available: <https://www.sciencedirect.com/science/article/pii/S0304399110003529>

- [24] F. Vurpillot, B. Gault, B. P. Geiser, and D. J. Larson, “Reconstructing atom probe data: A review,” *Ultramicroscopy*, vol. 132, pp. 19–30, 2013. [Online]. Available: <https://www.sciencedirect.com/science/article/pii/S0304399113000806>
- [25] Haley D., T. Petersen, S. Ringer, and G. Smith, “Atom probe trajectory mapping using experimental tip shape measurements,” *Journal of Microscopy*, vol. 244, no. 2, pp. 170–180, 11 2011.
- [26] Y.-T. Ling, S. Cools, J. Bogdanowicz, C. Fleischmann, J. D. Beenhouwer, J. Sijbers, and W. Vandervorst, “A Bottom-Up Volume Reconstruction Method for Atom Probe Tomography,” *Microscopy and Microanalysis*, vol. 28, no. 4, pp. 1102–1115, 2022.
- [27] A. C. Day, A. J. Breen, and S. P. Ringer, “A Crystallography-Mediated Reconstruction (CMR) Approach for Atom Probe Tomography: Solution for a Singleton Pole,” *Ultramicroscopy*, vol. 224, p. 113262, 5 2021.
- [28] A. C. Day, A. V. Ceguerra, and S. P. Ringer, “Introducing a Crystallography-Mediated Reconstruction (CMR) Approach to Atom Probe Tomography,” *Microscopy and Microanalysis*, vol. 25, no. 2, pp. 288–300, 4 2019.
- [29] D. J. Larson, B. P. Geiser, T. J. Prosa, S. S. A. Gerstl, D. A. Reinhard, and T. F. Kelly, “Improvements in planar feature reconstructions in atom probe tomography,” *Journal of Microscopy*, vol. 243, no. 1, pp. 15–30, 2011. [Online]. Available: <https://onlinelibrary.wiley.com/doi/abs/10.1111/j.1365-2818.2010.03474.x>
- [30] S. Adachi, “Silicon-Germanium Alloy (SixGe_{1-x})”, in *Optical Constants of Crystalline and Amorphous Semiconductors: Numerical Data and Graphical Information*. Boston, MA: Springer US, 1999, pp. 94–112. [Online]. Available: https://doi.org/10.1007/978-1-4615-5247-5_9
- [31] CAMECA, “IVAS 3.8.0 User Guide,” 2017.
- [32] “Gwyddion documentation, chapter 4: One-Dimensional Roughness Parameters.” [Online]. Available: <http://gwyddion.net/documentation/user-guide-en/roughness-iso.html>
- [33] J. M. Cairney, K. Rajan, D. Haley, B. Gault, P. A. Bagot, P.-P. Choi, P. J. Felfer, S. P. Ringer, R. K. Marceau, and M. P. Moody, “Mining information from atom probe data,” *Ultramicroscopy*, vol. 159, pp. 324–337, 12 2015.
- [34] B. Gault, M. P. Moody, F. de Geuser, G. Tsafnat, A. La Fontaine, L. T. Stephenson, D. Haley, and S. P. Ringer, “Advances in the calibration of atom probe tomographic reconstruction,” *Journal of Applied Physics*, vol. 105, no. 3, p. 034913, 2 2009.
- [35] A. J. Breen, M. P. Moody, A. V. Ceguerra, B. Gault, V. J. Araullo-Peters, and S. P. Ringer, “Restoring the lattice of Si-based atom probe reconstructions for enhanced information on dopant positioning,” *Ultramicroscopy*, vol. 159, pp. 314–323, 2015. [Online]. Available: <https://www.sciencedirect.com/science/article/pii/S0304399115001163>
- [36] N. D. Wallace, A. V. Ceguerra, A. J. Breen, and S. P. Ringer, “On the retrieval of crystallographic information from atom probe microscopy data via signal mapping from the detector coordinate space,” *Ultramicroscopy*, vol. 189, pp. 65–75, 2018. [Online]. Available: <https://www.sciencedirect.com/science/article/pii/S0304399117303650>

- [37] L. Yao, T. Withrow, O. D. Restrepo, W. Windl, and E. A. Marquis, “Effects of the local structure dependence of evaporation fields on field evaporation behavior,” *Applied Physics Letters*, vol. 107, no. 24, p. 241602, 12 2015.
- [38] V. J. Araullo-Peters, A. Breen, A. V. Ceguerra, B. Gault, S. P. Ringer, and J. M. Cairney, “A new systematic framework for crystallographic analysis of atom probe data,” *Ultramicroscopy*, vol. 154, pp. 7–14, 2015. [Online]. Available: <https://www.sciencedirect.com/science/article/pii/S0304399115000248>
- [39] L. Yao, M. P. Moody, J. M. Cairney, D. Haley, A. V. Ceguerra, C. Zhu, and S. P. Ringer, “Crystallographic structural analysis in atom probe microscopy via 3D Hough transformation,” *Ultramicroscopy*, vol. 111, no. 6, pp. 458–463, 2011. [Online]. Available: <https://www.sciencedirect.com/science/article/pii/S0304399110003086>
- [40] F. De Geuser, B. Gault, A. Bostel, and F. Vurpillot, “Correlated field evaporation as seen by atom probe tomography,” *Surface Science*, vol. 601, no. 2, pp. 536–543, 1 2007.
- [41] L. Yao, “A filtering method to reveal crystalline patterns from atom probe microscopy desorption maps,” *MethodsX*, vol. 3, pp. 268–273, 2016.
- [42] C. Oberdorfer, S. M. Eich, and G. Schmitz, “A full-scale simulation approach for atom probe tomography,” *Ultramicroscopy*, vol. 128, pp. 55–67, 2013. [Online]. Available: <https://www.sciencedirect.com/science/article/pii/S0304399113000144>
- [43] CAMECA, “Periodic Table of the Isotopes for Atom Probe Tomography.” [Online]. Available: <https://www.atomprobe.com/keyaptlinks/getyourperiodictable>